Journal of Materials Processing Tech. 352 (2026) 119303

Contents lists available at ScienceDirect

Journal of Materials Processing Tech.

journal homepage: www.elsevier.com/locate/jmatprotec

Research article

# In-situ investigation of precipitation kinetics and microstructural evolution during friction extrusion of the aluminium alloy AA7075

Elizabeth Mathew [a,*], Chang Yin-Cheng Chan [a], Lars Rath [a], Julian Escobar [b], Emad Maawad [c], Harikrishnasinh Rana [a], Uceu Fuad Hasan Suhuddin [a], Peter Staron [c], Jorge F. dos Santos [b], Benjamin Klusemann [a,d]

[a] *Institute of Material and Process Design, Helmholtz-Zentrum Hereon, Max-Plank-Straße 1, 21502 Geesthacht, Germany*
[b] *Pacific Northwest National Laboratory, Richland, 99352 WA, USA*
[c] *Institute of Materials Physics, Helmholtz-Zentrum Hereon, Max-Plank-Straße 1, 21502 Geesthacht, Germany*
[d] *Institute for Production Technology and Systems, Leuphana University Lüneburg, Universitätsallee 1, 21335 Lüneburg, Germany*

## ARTICLE INFO

*Keywords:*
WAXS
SAXS
AA7075-T651
Precipitation kinetics
Analytical model

## ABSTRACT

Microstructural evolution under severe thermo-mechanical conditions is challenging to characterize, particularly in precipitation-hardenable aluminium alloys where high strain rates and elevated temperatures promote precipitate dissolution, nucleation, and growth. Capturing these dynamic processes requires in-situ characterization techniques. In this work, a novel experimental setup for in-situ investigation of friction extrusion (FE) is introduced using the FlexiStir device, a portable friction stir unit designed for operation at high-energy synchrotron beamlines. Time-resolved measurements during friction extrusion of AA7075-T651 were successfully performed, enabling direct observation of precipitation and microstructural evolution during processing. The combined effects of frictional heating and severe plastic deformation on precipitation kinetics and grain refinement were analyzed, supported by an analytical model describing the temperature rise due to frictional heating. The results reveal a strong coupling between processing conditions and microstructural evolution. In particular, precipitates exhibit an approximately four-fold increase in size during processing, as confirmed by scanning transmission electron microscopy and small-angle X-ray scattering. In addition, recrystallization-driven grain refinement was characterized through detailed microstructural analysis. Lower applied forces were found to produce higher processing temperatures and longer thermal exposure, promoting grain growth and reducing precipitate retention after cooling. These findings establish a direct relationship between applied force, temperature evolution, and dynamic precipitation behavior during friction extrusion.

## 1. Introduction

Friction extrusion (FE) was developed and patented by TWI in 1993 [1]. The process follows a similar strategy as the conventional hot extrusion process, except for the rotation that is introduced to impart plastic deformation and consolidation of the feedstock material during the extrusion process. Even though this process came into existence three decades ago, only recently it has piqued the interest of the research community [2]. Recently, FE has emerged as an interesting process route to obtain tailored alloys by mechanical alloying, recycling of machining waste, and consolidation of powder products [3].

FE is a solid-state, friction-based processing technique that utilizes frictional heat and pressure generated by the die's relative motion. This frictional heating softens the material without reaching its melting point. Based on their applications, friction-based technologies are typically categorized into two groups: joining and processing [4]. Among joining processes, friction stir welding (FSW) [5] and refill friction stir spot welding [6] are well-known techniques that enable joining dissimilar materials considered non-weldable. Friction stir processing (FSP) [7], friction consolidation [8] and FE [2] can be classified as friction-based processing techniques. The frictional heating associated with all these processes softens the material without reaching its melting point, resulting in fine-grained microstructures due to dynamic recrystallization induced by severe plastic deformation at elevated temperatures. Moreover, since the temperature remains below the alloy's melting point, issues related to melting and solidification that affect mechanical properties are avoided [3]. FE is used to extrude solid or hollow structures from feedstock materials such as chips, powder, or

---

[*] Corresponding author.
*E-mail address:* Elizabeth.Mathew@hereon.de (E. Mathew).

https://doi.org/10.1016/j.jmatprotec.2026.119303
Received 5 February 2026; Received in revised form 21 March 2026; Accepted 29 March 2026

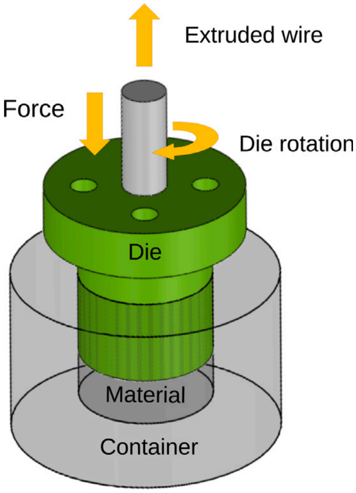

**Fig. 1.** Schematic illustration of the Friction Extrusion (FE) process, in which combined rotational and axial forces are applied to the material within a container, generating frictional heat that softens the material and enables its extrusion through a die orifice to form a wire.

bulk material. An advantage compared to conventional hot extrusion is that FE requires lower force, and the localized heating due to friction helps save energy and time by eliminating the need for preheating [9]. Additionally, FE wires could be utilized in friction-based additive manufacturing, such as friction surfacing [10] or Additive Friction Stir Deposition [11]. The schematic of the FE process is shown in Fig. 1. FE involves a container containing the material to be extruded and a revolving die that is subjected to the applied force. The plasticized layer develops in close proximity to the die and has a restricted thickness, referred to as the forming zone. The flow of material is constrained by an orifice inside the die, which controls the extrusion process [9].

Several studies have investigated the processing of aluminium alloys using FE. For instance, Tang et al. [2] showed the extrusion of AA2050 alloy and AA2195 chips using FE, resulting in fully recrystallized and equiaxed grains, where the grain size increased as a function of rotational speed. Baffari et al. [12] studied the effect of process parameters on AA2050 and found that higher rotational speed and extrusion force result in abnormal grain growth and hot cracking due to excessive frictional heating. Halak et al. [13] investigated the effect of extrusion force and observed that with an increase in force, the initially only outer refined region increased, even though the processing time decreased. The studies also looked into the effect of die angle, where, with a higher force at a die angle of 60°, a completely recrystallized wire with ultrafine grains was produced at a low extrusion ratio. Li et al. [14] studied the strain and texture of the FE wire. Wang et al. [15] studied the evolution of microstructure from the extruded wire to the base material. They found that high grain refinement was achieved near the extrudate region due to discontinuous dynamic recrystallization (DDRX) indicated by the presence of larger amount of high angle grain boundaries (HAGBs). However, for the central part, there was grain fragmentation due to strain accumulation, shown by the higher frequency of low angle grain boundaries (LAGBs). While previous studies have demonstrated that FE can produce fully recrystallized microstructures in aluminium alloys, the reported grain evolution strongly depends on processing parameters such as rotational speed, extrusion force, and die geometry. However, most studies have primarily emphasized the role of rotational speed, whereas the influence of extrusion force on microstructural evolution and recrystallization behavior remains insufficiently understood. Therefore, a comprehensive understanding of how extrusion force influences the dynamic recrystallization behavior and microstructural evolution during FE remains limited. Addressing this knowledge gap is essential for optimizing FE process parameters and controlling the microstructure of extruded aluminium alloys.

Besides grain size, precipitates are crucial in many aluminium alloys since their presence directly affects the properties. For example, Whalen et al. [16] showed for extruded Al powder twice the elongation, with similar high yield strength caused by grain size reduction and formation of secondary nanoscale phases in comparison to conventional hot extrusion. Kalsar et al. [17] found homogeneously distributed stable $\eta$ ($MgZn_2$) precipitates in AA7075 after FE, resulting in a higher surface-to-volume ratio and improved aging response. However, most of these studies have characterized the microstructure and grain size using ex-situ analysis and primarily focused on variations in die geometry and processing parameters. Typically, transmission electron microscopy (TEM) is employed to investigate precipitates, which is challenging especially with respect to the sample preparation. Additionally, the analysis is limited to a small region. To overcome this problem, small angle X-ray scattering (SAXS) and wide angle X-ray scattering (WAXS) are utilized to study the precipitate size distribution and the precipitate phases, respectively, of a larger volume. Even though TEM studies help to understand the final properties after processing, they fail to capture the dissolution of precipitates while the process is happening. Moreover, precipitates can coarsen or dissolve during processing, making it difficult to accurately interpret their evolution after processing. Thus, to understand the microstructural evolution during processing, such as when the die is extruding the material during FE, there is a need for real time analysis.

In this study, the alloy AA7075 is utilized. It is a precipitation hardenable alloy, meaning that its mechanical properties are determined by the shape and distribution of fine, coherent precipitates and dispersoids. The 7xxx series aluminium alloys are of particular interest due to their widespread use in lightweight aerospace applications, owing to their high strength-to-weight ratio, good machinability, excellent fracture toughness, and affordability [18]. Moreover, AA7075 alloys tend to recover at room temperature due to natural aging [19], making real time analysis crucial. One possibility to obtain in situ information during complex thermo-mechanical processes is to simulate them via a dilatometer. For instance, Henninger et al. [20] simulated friction stir welding (FSW) experiments using a quenching dilatometer to understand the influence of temperature and welding speed on the precipitation evolution using SAXS and X-ray diffraction (XRD). However, such physical simulations are limited to simplified thermo-mechanical conditions and cannot fully capture the complex deformation and heat generation occurring in the actual process. To obtain insight into the actual process, the analysis has to be performed in situ during processing. Up to now, also due to its complexity, in-situ studies on friction-based processes are rather limited. Woo et al. [21] investigated the temperature and stress evolution of AA6061-T6 during FSW using neutron diffraction via a remotely operated portable FSW machine. Up to now, there exists only one in-situ study on precipitation kinetics during FSW using synchrotron radiation by dos Santos et al. [22], showing for AA7449-TAF the complex transformation, dissolution and reprecipitation that happened during welding. This investigation has been made possible by utilizing the FlexiStir device [22] that can be installed in a synchrotron X-ray beamline and allows for the acquisition of microstructural data using SAXS and WAXS during welding.

Despite these advances, in-situ investigations of FE remain unexplored, and the relationship between process force, temperature evolution, and dynamic precipitation behavior during FE is still poorly understood. In particular, while extrusion processes involve strong material confinement and force-controlled deformation, the influence of extrusion force on precipitation kinetics and microstructural evolution has not yet been investigated in real time. Therefore, the present study introduces a novel experimental approach for the first in-situ investigation of friction extrusion using the FlexiStir device. Unlike FSW, where the material is not fully confined and tool rotation and surface

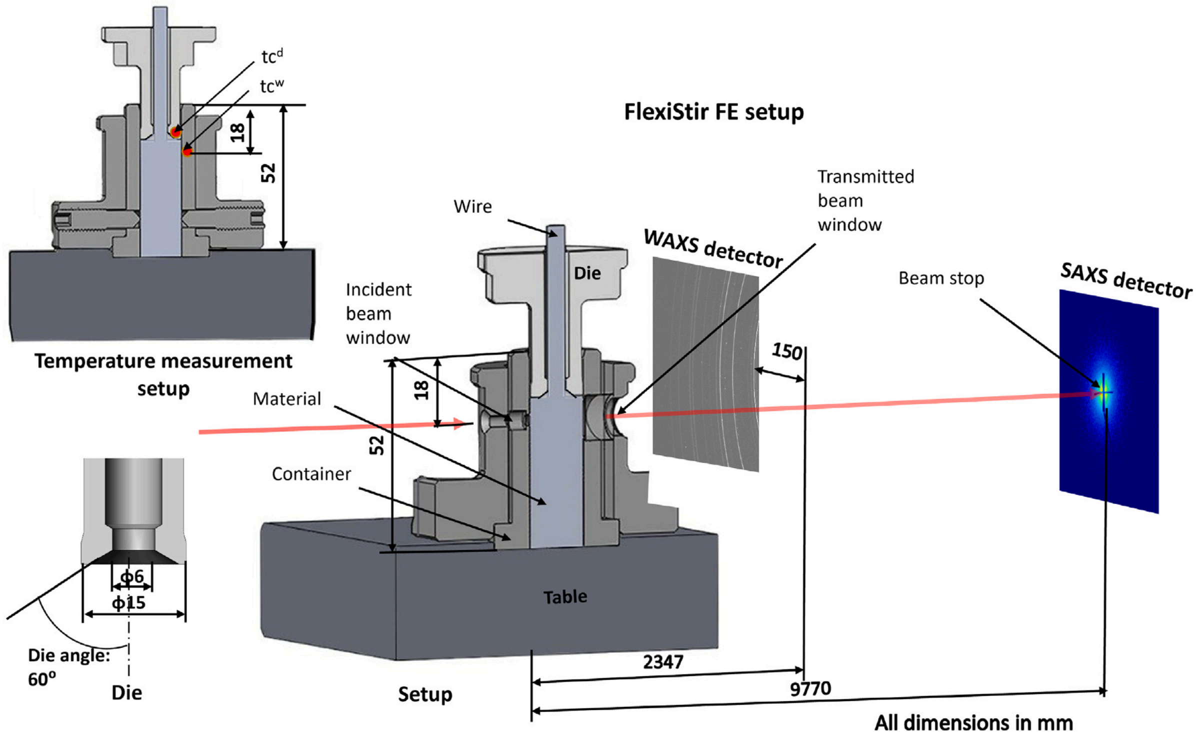

**Fig. 2.** Schematic illustration of the FE setup at the synchrotron, including the die angle used and the front view of the FlexiStir setup aligned with the incident beam direction. The thermocouple positions used for ex-situ temperature measurements are referred to as $tc^w$ located at the center of the window and $tc^d$ located in the die.

**Table 1**
Chemical composition (in wt%) determined with Optical Emission Spectroscopy (OES) of the used AA7075-T651 material.

| Si | Fe | Cu | Mn | Mg | Cr | Zn | Ti | Ni | Sn | Zr | Al |
|---|---|---|---|---|---|---|---|---|---|---|---|
| 0.08 | 0.13 | 1.6 | 0.03 | 2.6 | 0.16 | 6.0 | 0.04 | 0.01 | 0.01 | 0.02 | Bal. |

conditions strongly influence the process, FE involves confined material flow where the applied force plays a dominant role in determining the thermo-mechanical conditions. In this work, AA7075 is extruded using a die angle of 60° at two different extrusion forces to investigate the effect of force on temperature evolution, precipitation kinetics, and microstructural development. The experiments are performed using in-situ synchrotron SAXS and WAXS, enabling direct observation of precipitation behavior during and after FE for the first time.

## 2. Experiment and data analysis

### 2.1. Material

This study employed a commercial AA7075 alloy in T651 temper as the base material. The results of the material's chemical composition measurement at Material Services GmbH using optical emission spectroscopy (OES) are shown in Table 1. Bulk billets of 15 mm diameter and 45 mm in height have been utilized.

### 2.2. Friction extrusion process using FlexiStir

The FlexiStir system, a special device created to carry out in-situ sychrotron X-ray scattering experiments initially intended for FSW [22], was used to perform for the first time an in-situ FE process investigation. The container stayed still during extrusion, where the die rotated during the penetration of the material. The detailed setup for the experiment is displayed in Fig. 2.

The container used in this study has a dimension of 52 mm height with an inner diameter of 15 mm and a wall thickness of 5 mm in the relevant part. The corresponding die has 15 mm outer diameter, featuring a die angle of 60° with an internal die orifice of 6 mm, resulting in an extrusion ratio of 6.25. Both parts were manufactured from AISI 4140 steel. Additionally, the setup includes two windows made of sapphire glass around the beam axis, 18 mm from the top of the container. The first, located at the beam entry point, has a diameter of 5 mm and a thickness of 5 mm; the second, positioned in the transmission region, has a diameter of 12 mm and a thickness of 8 mm. The difference in diameter accounts for the beam that enters the sample and after undergoing scattering needs a wider outlet to reach the detectors. The window thickness is a result of handling requirements and anticipated peak load; but failure frequently happened at the end of the process owing to thermal shock, which had no discernible effect on the SAXS/WAXS signal. The effect of the observed damage on the SAXS measurements is negligible, as SAXS probes nanoscale features and is not significantly affected by minor surface damage or artifacts. Therefore, the reliability of the SAXS data remains unaffected. However, sometimes sapphire glass artifact and Debye–Scherrer rings were seen on the 2D images, see Appendix A. Furthermore, diffraction and SAXS measurements showed no problems with background, and the sapphire glass exhibited high X-ray transmission, allowing sufficient beam intensity to reach the detector. The position of the X-ray beam was kept constant throughout the experiments. Although FlexiStir can be tilted, as was done for the FSW study by dos Santos et al. [22], it was kept parallel to the beam and not tilted in the present FE experiments. Moreover, temperature measurements were conducted ex-situ, and the positions of the K-type thermocouples are shown in the front view in Fig. 2. Thermocouple $tc^w$ is positioned 18 mm from the top of the container (aligned with the window) and 1 mm below the container surface, while $tc^d$ is located at 2/3 of the radius from the center of the die and 1 mm below the die surface. The original spindle motor is connected to a gearbox that delivers a torque of 450 N m and a

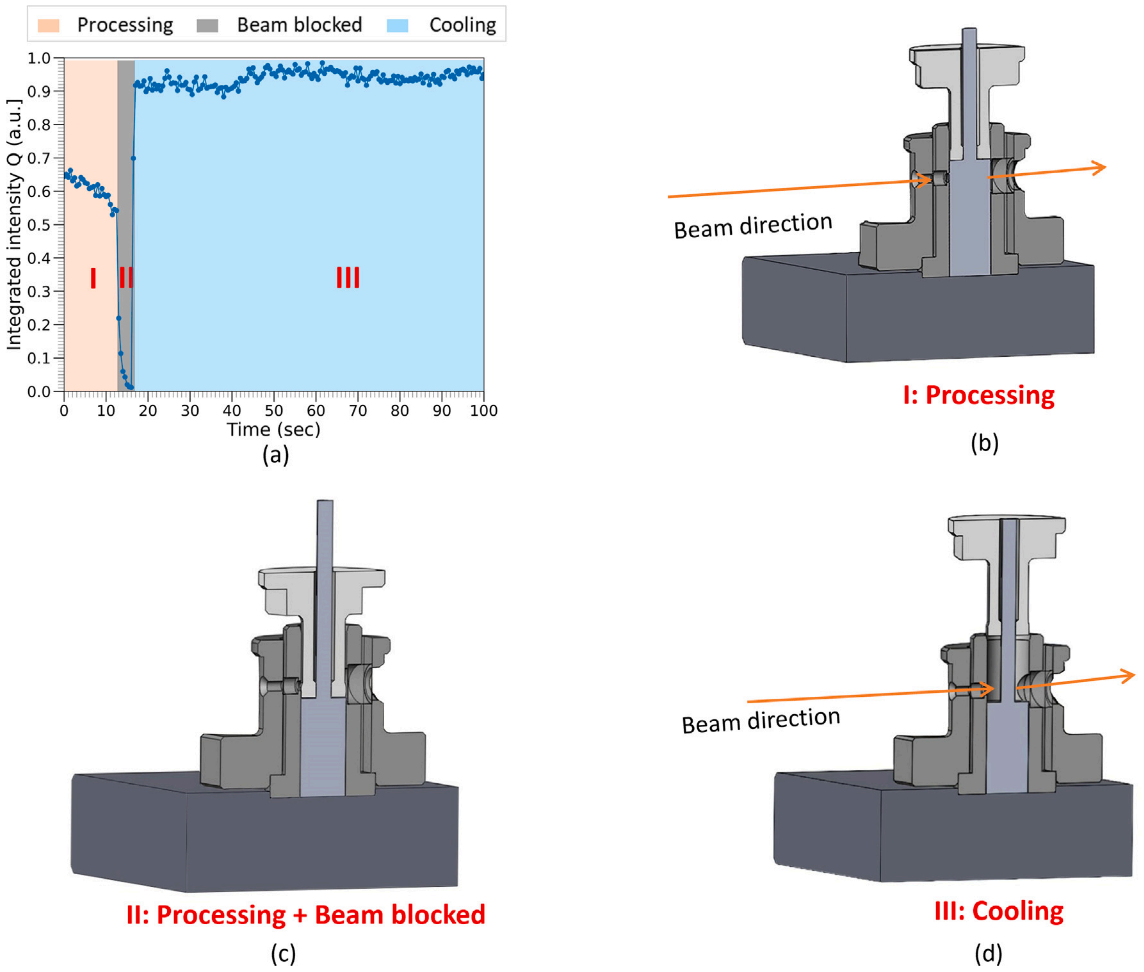

**Fig. 3.** (a) Intensity as a function of time, with different stages during FE marked as Case I, II, and III; (b) Schematic of the processing stage showing beam transmission through the base material (15 mm thickness); (c) Schematic of the processing stage where the beam is blocked; (d) Schematic of the cooling stage showing beam transmission through the extruded wire (6 mm thickness).

**Table 2**
Process parameters of FE for the AA7075 alloy.

| Process name | Rotation speed [rpm] | Die angle [°] | Force [kN] |
|---|---|---|---|
| FE-16 | 300 | 60 | 16 |
| FE-22 | 300 | 60 | 22 |

**Table 3**
Transmission of the beam through sapphire windows ($T_w$), sample ($T_s$), and the final transmission through both the sample and the windows ($T_{sw}$) during processing (thickness = 15 mm) and after extrusion (thickness = 6 mm).

| Thickness [mm] | $T_w$ [%] | $T_s$ [%] | $T_{sw}$[%] |
|---|---|---|---|
| 15 | 59 | 19 | 11 |
| 6 | 59 | 33 | 19 |

rotational speed of 600 rpm, with a maximum axial force capacity of 40 kN.

For the current study, the process parameters employed are shown in Table 2. During the process, the die was plunged 13 mm into the AA7075 billet, ensuring that the beam is going through the wire after processing. However, this resulted in the fact that the signal was blocked in the last few seconds of processing, as the die was in front of the window, see Fig. 3c. The in-situ measurements are limited by the constraints of the FE setup, as die motion causes beam obstruction near the end of processing because the beam position cannot be adjusted. In addition, accessing the extruded wire through the window for subsequent characterization would require further die plunging, which would block the beam. The length of the wires produced after the process is roughly 77 mm. The complete setup cooled down at air for approximately 900 s.

The beam needs to penetrate 15 mm during processing and 6 mm after extrusion of the AA7075 alloy, in addition to passing through the sapphire glass windows (8 mm + 5 mm). Therefore, a high photon energy is needed, which is available at the high-energy materials science beamline P07 at PETRA III, operated by Helmholtz-Zentrum Hereon at Deutsches Elektronen-Synchrotron (DESY), Germany. Table 3 provides details on the transmission through the sapphire windows ($T_w$), the sample (AA7075) ($T_s$), and the final transmission through both the sample and the windows during processing and after extrusion ($T_{sw}$). One benefit of having such a high photon energy is that the experiment can be carried out in air without the need for a vacuum. The drawback is that the range of covered scattering vectors is restricted at the small q end of the scattering curve (0.04 $\text{nm}^{-1}$ to 3.2 $\text{nm}^{-1}$), which depends on the photon wavelength ($\lambda = 0.169$ Å).

### *2.3. Experimental setup and data analysis for in-situ SAXS and WAXS during friction extrusion*

#### *2.3.1. SAXS*

The SAXS signals were recorded using a PILATUS3 X CdTe 2M detector with a pixel size of 172 μm *x* 172 μm at a distance of 9.7 m from the sample, calculated using the calibrant silver behenate (AgBH). During the FE experiments, detector images were collected continuously with an exposure time of 0.5 s. This exposure time was sufficient to capture the precipitate dissolution. At a known heating rates of 15–30 °C $s^{-1}$ for the FE process under the studied process parameters, this corresponds to 7.5–15 °C per frame. Given that precipitate dissolution occurs over a broad temperature interval of $\geq$ 80 °C, see Fig. 5a, the temporal resolution was adequate to capture the phase evolution. After the process, the cooling phase was also studied to understand natural aging. The pyFAI module [23] in Python was used to azimuthally integrate the scattering signal. The scattering images underwent azimuthal integration because the scattering signals obtained during the experiment were isotropic.

Fig. 3a shows the scattering intensity at q = 0.5 $nm^{-1}$ as a function of time. Clearly, the scattering intensity has three distinct regions. These regions can be explained by the path through which the beam was transmitted through the sample, separated into three cases as follows. In Case I, as illustrated in Fig. 3b, the FE process is being carried out, and the X-ray beam still passes through the billet; thus, the thickness of the sample to be penetrated is 15 mm. This resulted in lower intensity reaching the detector during the processing time in comparison to the cooling stage. Fig. 3c shows Case II, where the signal is being completely blocked by the die, resulting in nearly no signal reaching the detector. This is an inherent constraint of the friction extrusion setup required to access the wire for cooling characterization. This truncation is a systematic limitation rather than an experimental error. Hence, the WAXS/SAXS images recorded during this time were not analyzed. Case III, as shown in Fig. 3d, is the cooling stage where the die has been completely retracted, and the X-ray beam is going through a smaller thickness of 6 mm of the extruded wire. This case starts after the processing period and the removal of the die. The scattering intensity obtained from Case III is higher than in Case I.

Calibration of the scattering curves to an absolute macroscopic scattering cross-section ($sr^{-1}cm^{-1}$) is required for determining the precipitate volume fraction. This calibration was performed using glassy carbon as a Ref. [24]. Additionally, the X-ray transmission values measured before and after the process, see Table 3, were taken into account to accurately determine the absolute macroscopic scattering cross-section. Fig. 4 shows scattering curves at different times after calibration for both Case I and Case III regions. The scattering curves were fitted, based on the assumption that the system is dilute, and the precipitates are non-interacting with a known shape function and log-normal dispersion model. The main strengthening phase is $MgZn_2$ ($\eta$) for 7075-T651 [25]. Other precipitates were neglected, see Section 3.1. The scattering curves from 0.04 $nm^{-1}$ to 1.3 $nm^{-1}$ were fitted to a log-normal distribution with a background. This corresponds to real-space dimensions of approximately should be −157 nm, allowing reliable detection of particles up to 120 nm in diameter. The precipitates were assumed to be ellipsoids of revolution with an aspect ratio of 0.4. Their composition was taken at equilibrium, with a density of 5.09 $g/cm^3$, resulting in a scattering contrast of $1.8 \times 10^{10}$ $cm^{-2}$ with respect to the aluminium matrix [20].

### 2.3.2. WAXS

The WAXS data was recorded using a Perkin Elmer XRD 1621 Flat Panel detector with a detector distance of 2.3 m and a pixel size of 200 μm × 200 μm. The calibration was done using $LaB_6$. The range of the $2\theta$ scattering angles that were examined was 4.3° to 13.7°. To enable simultaneous SAXS and WAXS signal acquisition during processing, the WAXS detector was laterally displaced by 150 mm, as illustrated in Fig. 2. As a result of this offset position, only a partial segment of the Debye–Scherrer rings was captured in the WAXS patterns.

Integrations were carried out using the Pydidas software [26]. WAXS signals were utilized to obtain the d-spacing in order to calculate the temperature along the beam direction. The equilibrium phase fraction as a function of temperature was calculated using the PanAluminium database in the PANDAT software [27,28].

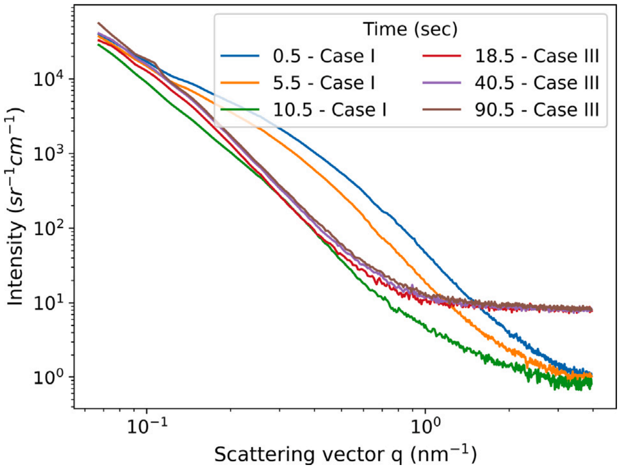

**Fig. 4.** Measured small angle X-ray scattering (SAXS) curves at different times (in sec) throughout the process FE-22. Case I represents the processing stage, and Case III is the cooling stage, see Fig. 3.

### 2.4. Microscopy and microhardness testing

The extruded wire and the residual material were sectioned, ground and polished according to standard metallographic preparation procedures. The samples for optical microscope observation were etched with Barker's Reagent and observed with a Keyence VHX-6000 digital microscope and a Leica DMi8 optical microscope equipped with polarized light. Furthermore, the microstructure was analyzed at specific regions by a Thermo Fisher Quanta 650 field emission gun scanning electron microscope (SEM) equipped with a Velocity electron backscatter diffraction (EBSD) system. The data from EBSD were analyzed by TSL OIM. A misorientation angle of 15 degrees (°) was utilized to differentiate the LAGBs and HAGBs. A minimum misorientation angle of 2° was applied to eliminate spurious boundaries. The recrystallization grain volume fraction was evaluated using the Grain Orientation Spread (GOS), where grains with intragranular misorientation lower than 2° was identified as recrystallized grains.

Precipitate size measurements were conducted in Thermo Fisher Talos F200i TEM via scanning transmission electron microscopy (STEM) operated at 200 kV. The TEM lamella was milled utilizing Ga+ focused ion beam (FIB) equipped in Thermo Fisher Nova-200 dual bean SEM.

Microhardness were measured with an EMCO-TEST Durascan 70 G5 automated hardness testing machine with a load of 0.2 kgf at the end of the extruded wires. A two dimensional hardness map was generated with a grid size of 0.5 mm, covering the entire sample along the radial direction and comprising 3 measurement points along the extruded direction. This region corresponded to the area observed during the in-situ FE experiments.

## 3. Results

In the FE process, an extruded wire is obtained after AA7075-T651 undergoes significant plastic shear deformation and frictional heating, resulting in a very refined grain structure. The frictional heating, which influences the grain microstructure evolution as well as the formation of precipitates, is directly influenced by process parameters such as applied force. Next to thermocouple measurements, WAXS was used to calculate the temperature in the scanned volume during the process. Furthermore, SAXS was employed to investigate the evolution of precipitate size and volume fraction over time.

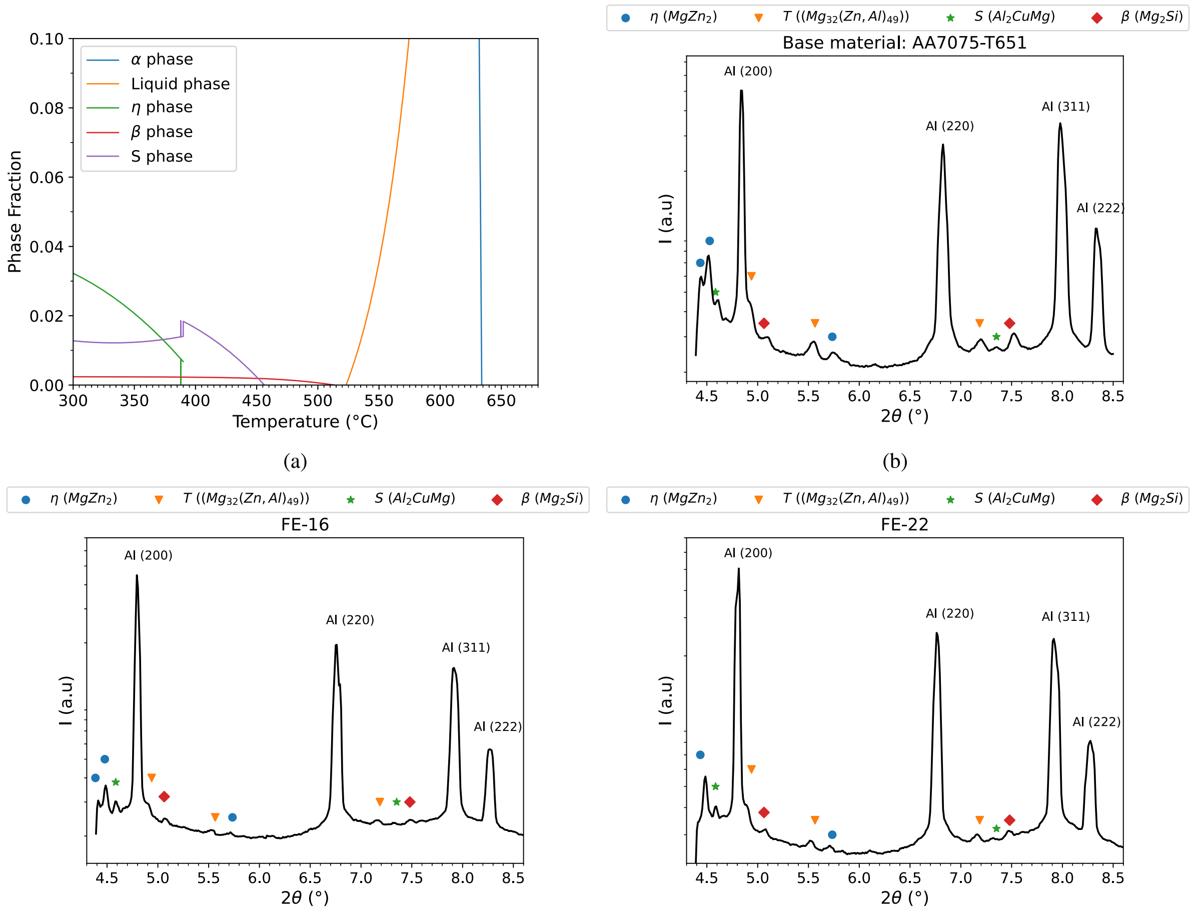

(a)

(b)

(c)

(d)

**Fig. 5.** (a) Equilibrium phase fractions as a function of temperature for the base material AA7075; (b) X-ray diffractogram of base material AA7075-T651; (c) Diffractogram after FE processing for FE-16; (d) Diffractogram after FE processing for FE-22.

### 3.1. Evolution of WAXS diffractograms during FE

Fig. 5a shows the equilibrium phase fractions as a function of temperature for the base material AA7075 obtained from PANDAT [27]. From the diffraction pattern shown in Fig. 5b, it is evident that precipitates of the $\eta$ (MgZn$_2$) phase, T (Mg$_{32}$(Zn,Al)$_{49}$) phase, S (Al$_2$CuMg) phase and $\beta$ (Mg$_2$Si) phase are already present in the AA7075-T651 base material. The equilibrium $\eta$ phase has a hexagonal crystal structure (space group = P6$_3$/mmc; a = 5.223 Å and c = 8.566 Å) [29]. $T$ phase has a cubic crystal structure (space group = Im-3; a = 14.16 Å) [30]. Furthermore, the precipitate size of $T$ phase is greater than 100 nm [31]. The structure of the $\beta$ (Mg$_2$Si) phase is cubic (space group: Fm-3 m; a = 6.35 Å). According to Pan et al. [32], the primary $\beta$ phase forms dendritic structures that are around 30 μm in size and have a polygonal shape and are mostly considered as secondary phases. S phase is another secondary phase (space group = Cmcm; a = 4.01 Å; b = 9.3 Å; c = 7.15 Å) [33]. The T, S and $\beta$ precipitates were not included in the SAXS analysis since their sizes are outside the Q-range, which is the observable range of the current SAXS measurements. Another important strengthening phase in the AA7075 alloy is the $\eta'$ phase, which has a hexagonal crystal structure (a = 4.96 Å, c = 14.03 Å) [34]. These precipitates are extremely small and do not create observable diffraction peaks, hence are not observed in Fig. 5b. $\eta'$ phase forms a fine dispersion (diameter = 5–6 nm), along grain boundaries and dislocations [25]. Moreover, the equilibrium $\eta$ phase gradually replaces the metastable $\eta'$ phase. The standard precipitation sequence in alloys of the 7xxx series is: Supersaturated solid solution ($\alpha$) → GP zones → $\eta'$ → $\eta$ [34]. The absence of detectable $\eta'$ reflections in the diffraction patterns prevented a separate analysis of its evolution during the FE process. In the SAXS analysis, the scattering signal represents the overall population of nanoscale precipitates [22]. However, the method does not allow a clear distinction between different precipitate types such as $\eta'$ and $\eta$. Therefore, the SAXS results provide information on the overall precipitation and dissolution behavior, but a phase-specific quantification of $\eta'$ precipitates during the FE process is not possible.

As shown in Fig. 5a, under equilibrium conditions for the AA7075 composition, the $\eta$ phase is fully dissolved at approximately 390 °C, whereas the S phase begins to dissolve at a higher temperature of around 460 °C in the base material. The $\beta$ phase remains stable until about 480 °C and then fully dissolves at 510 °C, which is close to the FE processing temperature. Neither the $T$ phase nor the $\eta'$ phase was observed thermodynamically in Fig. 5a, likely because both are considered metastable. Additionally, the formation of the $T$ phase depends on the alloying elements content, i.e. low Cu and high Mg [35]. However, the AA7075 base material contains higher Cu and lower Mg, which favors the formation of the S phase over the $T$ phase under equilibrium conditions. Finally, as illustrated in Fig. 5c,d, no phase changes were detected in the WAXS signal after FE processing. Consequently, no transformation and new phase formation was considered for the SAXS analysis of precipitates.

Fig. 6a,b show the decrease in peak intensity as a function of time of the $\eta$ phase (201) at $2\theta$ = 4.43°. This particular peak was selected because it exhibits the highest intensity among the $\eta$ reflections. In both cases, a gradual reduction in the $\eta$ (201) intensity is observed as the process progresses. Towards the end of the process, just before the beam signal is completely blocked, the intensity approaches the

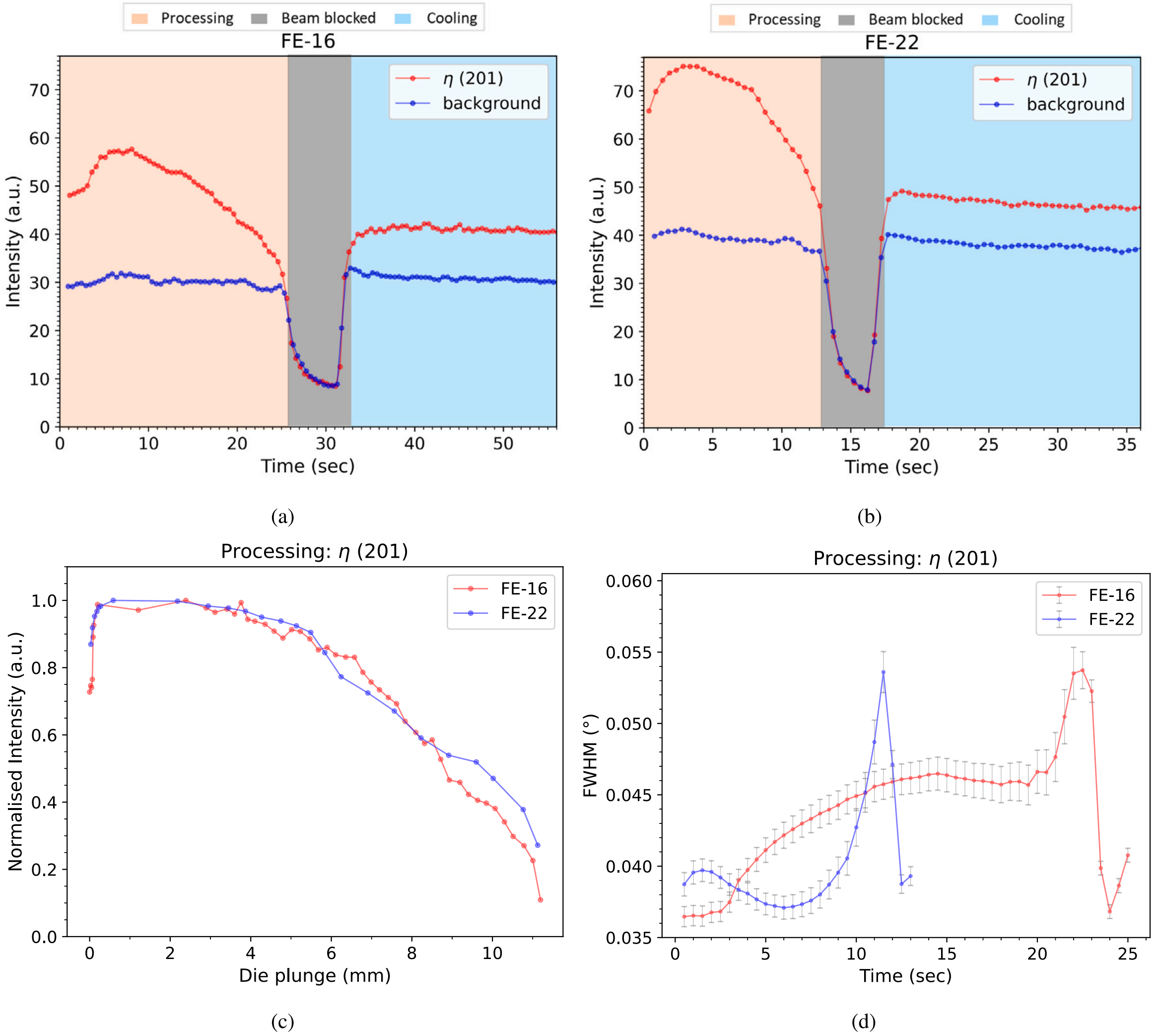

(a)

(b)

(c)

(d)

**Fig. 6.** Wide angle X-ray scattering (WAXS) evolution of the *η*-phase (201) reflection during FE: (a) Intensity evolution for FE-22 as a function of time; (b) Intensity evolution for FE-16 as a function of time; (c) Comparison of both processing conditions (FE-16 and FE-22) during die-plunge, with the background subtracted from the *η* (201) reflection and the intensity is normalized by setting the most intense peak to 1; (d) Evolution of the FWHM of the *η* (201) reflection as a function of time during processing.

background level. However, the peak does not fully disappear into the background, indicating that some *η* precipitates still remained near the end of the process. It is likely that with continued processing and further temperature increase, these precipitates would dissolve more into the matrix. The dissolution of *η* could not be captured completely due to the beam being blocked by the die, as shown in Fig. 3c. Additionally, the period during which the signal was blocked is marked by regions of zero intensity, occurring from approximately 13 to 17 s for the FE-22 process and from 26 to 33 s for the FE-16 process. Fig. 6c shows a comparison of both processing conditions (FE-16 and FE-22), where the background has been subtracted from the *η* (201) reflection and the data normalized by setting the most intense peak to 1. This was done to ensure that the peak intensity reflects only the *η* precipitate signal and not the contributions from the background. In both processes, the *η* precipitates dissolve as the die penetrates. However, the dissolution occurs more rapidly for FE-22, the process performed at a higher applied force, leading to a shorter processing time, see Fig. 7. In this regard, FE-16 shows a lower remaining signal compared to FE-22, suggesting a greater extent of *η* dissolution in FE-16 due to the longer processing time. The evolution of the FWHM of the *η* (201) reflection is shown in Fig. 6d. The FWHM initially increases, which can be attributed to deformation-induced microstrain and lattice distortion during processing. At later stages, a pronounced decrease in FWHM is observed, likely related to recovery or dynamic recrystallization processes at elevated temperature, which reduce dislocation density and lattice strain [36]. Such behavior is commonly reported in diffraction studies, where peak broadening is associated with deformation-induced strain and peak narrowing with strain relaxation during thermal recovery or annealing [37]. While these processes affect peak broadening, they do not directly change the phase fraction. Therefore, the continuous decrease in *η* phase peak intensity is primarily attributed to precipitate dissolution, which is further supported by the independent SAXS results.

### *3.2. Process behavior and temperature evolution via in-situ WAXS and ex-situ thermocouples during FE*

Fig. 7 shows the velocity, force, and temperature recorded during the FE processes. The temperature was estimated using both the lattice parameter expansion from the WAXS signal and recorded using the thermocouples located at the window ($tc^w$) and die ($tc^d$), respectively. Details of temperature calculation from WAXS data are provided in Appendix B. A preheating at 2 kN for 3 s to prevent torque spikes that could damage the machine and to establish good contact between die and material was performed before the actual extrusion force was applied. A subsequent force ramp up to the preset extrusion force

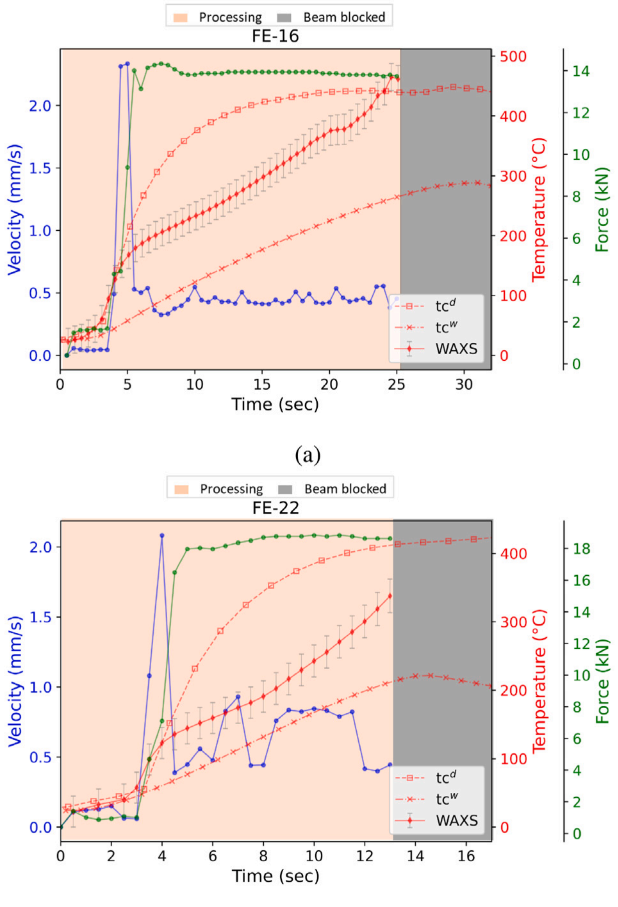

(a)

(b)

**Fig. 7.** Process behavior during friction extrusion: (a) FE-16 and (b) FE-22. Shown are force and velocity over time, along with temperature evolution measured via thermocouples positioned at the die (tc$^d$) and window (tc$^w$) (positions indicated in Fig. 2), as well as the temperature derived from the WAXS-based lattice parameter expansion that was measured through the windows.

within 1 s initiates the extrusion. During the force ramping, a spike in velocity was observed, indicating that the base material was upsetting and filling the cavity between the material and the die due to the 60° die geometry. A slightly lower extrusion force in FE-22 and FE-16 was present with the attained forces of 17.8 kN and 14 kN, respectively, which remain approximately constant throughout the processes. These lower forces are likely related to the low extrusion ratio (6.25), which reduces resistance and prevents the system from sustaining the targeted force. This indicates a slow controller response for the dynamic process. Another aspect is the axial force vibrations induced by tool rotation, which may further lower the average applied force, since force amplitudes above the threshold are naturally cut off due to the maximum acceleration limits imposed by the control system or the drives.

During both FE processes, the continuous temperature rise was observed in all three temperature measurements, although at different heating rates. The temperature determined via WAXS shows a rapid increase at the ramping stage, followed by a slow but continuous temperature increase. Meanwhile, the die temperature exhibits a similar rapid increase of temperature followed by a saturation of the temperature towards the end of the process. In contrast, the window temperature exhibits a more constant heating rate, which is slightly lower in comparison to the WAXS measurements. The discrepancy between the die and window temperatures is attributed to the different distance to the heat source at the die-material interface. Therefore, the window temperature experiences a more gentle increase due to a longer thermal diffusion length. The WAXS temperature lies between the die and window temperatures. This is because aluminium, as a feedstock material, has higher thermal conductivity than the surrounding steel container, influencing the local heat distribution. For instance, the center of the material experiences an earlier temperature increase in comparison with the corner. Recalling the transmitted WAXS signal, which examined the whole thickness of the feedstock material, a temperature higher than the window temperature is expected. The WAXS temperature in FE-22 is approximately 197 °C higher than tc$^w$ thermocouple measurement, while for FE-16 it is 148 °C higher than tc$^w$, both exceeding the corresponding tc$^w$ measurements at the outer region. This quantitative difference confirms that the material center undergoes an earlier and higher temperature rise, indicating the presence of a radial temperature gradient during friction extrusion. Nonetheless, the continuous increase in temperature simultaneously decreases the material's flow stress, making it easier to flow and leading to a higher extrusion rate. This increase in temperature aligns well with previous observations in FE studies [8,13] that heat is continuously generated during the process. However, FE being a thermo-mechanical process, the change in the lattice constant during the process can be attributed to elastic strain and thermal strain [21]. Therefore, the WAXS temperature needs a correction; however, this correction is small compared to the thermal strain, see Appendix C.

Although the WAXS gauge volume samples a localized region, this region progressively approaches the die-material interface towards the final stage of the process. At that point, however, the WAXS signal is lost due to the die blocking the signal. Therefore, direct diffraction measurements at the exact die interface are not available. To complement this limitation, thermocouples embedded in the die provide direct measurements of the local die temperature, which reflect the frictional heat generation at the interface. The WAXS measurements, on the other hand, capture the thermo-mechanical response within the adjacent material volume near the observation window. Together, these measurements allow assessment of how heat generated at the die interface propagates towards the sampled region, enabling a consistent interpretation of local heat generation and microstructural evolution. The differences in process temperature as well as processing time are affecting the recrystallization and precipitation kinetics. Therefore, SAXS was employed to investigate precipitate evolution under both force conditions. At the same time, SEM-EBSD and TEM were used to characterize the precipitate size after processing.

### 3.3. Macro- and microstructural analysis of extruded wires

The quality of the extrudate in terms of the surface appearance, external and internal defects are critical to evaluate the extrusion process parameters. Fig. 8 illustrates the outer surface, cross-sectional macrostructure in the extruded wires, as well as the transitional region from base material to extruded wire. Both processing parameters led to sound, continuous extruded wires without visible core defects, demonstrating the feasibility of the newly developed in-situ friction extrusion set-up. Extensive grain refinement initiates ahead of the die-material interface, see Fig. 8b,g, indicating the shear deformation propagates into the base material during extrusion. Distinct microstructures are observed at the center and the edge of extruded wire, see Fig. 8c,h. At the center of the wire, Fig. 8d,i, elongated grains showing a minor clockwise rotation along the extrusion direction are evident, whereas the equiaxed grains were observed at the edge, Fig. 8e,j, suggesting the grain refinement was not complete for the whole extruded wire. The presented equiaxed refine grains are likely associated with enhancing the ductility of the extruded wire [16]. The average grain sizes at the edges, calculated by the interception methods, are 3.2 μm and

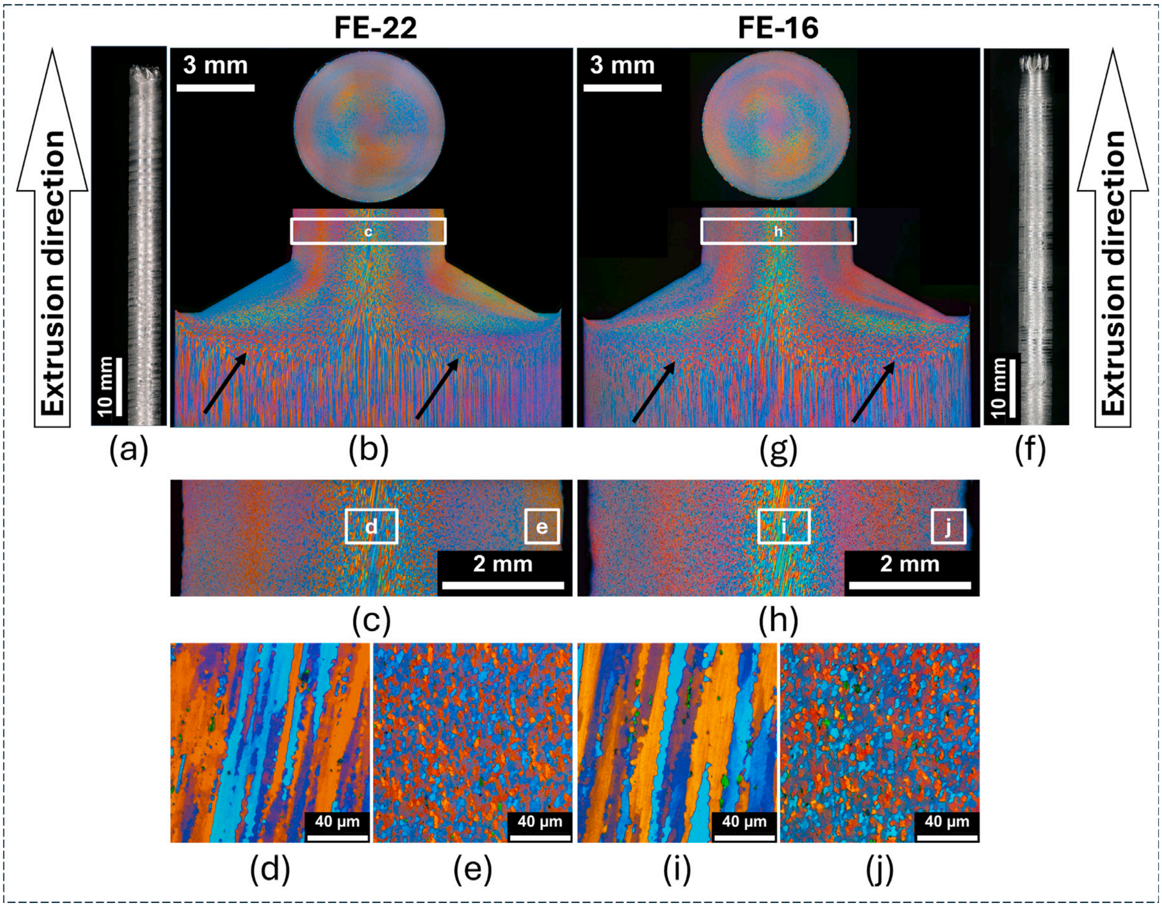

**Fig. 8.** Wire appearance and microstructure of the FE-22 (a–e) and FE-16 (f–j) samples. Optical micrographs of the appearance of (a) FE-22 and (f) FE-16 extruded wires. The transverse cross section of each extruded wire is shown in the upper part of (b) and (g), and the lower part is the residual billet ahead of the extrusion orifice. The black arrows indicate the initiation of extensive grain refinement. (c) and (h) display the longitudinal cross section of the extruded wires. The center and the periphery of the longitudinal cross section in FE-22 and FE-16 are presented in (d) and (e) as well as (i) and (j), respectively.

3.3 μm in FE-22 and FE-16, respectively. At constant rotation speed, dynamic recrystallization is enhanced at higher force due to higher shear deformation input. On the other hand, lower force results in higher heat input due to longer processing times, Fig. 7, which will promote grain growth and diminish grain refinement [12]. Despite the increased heat input observed at lower processing force, the absence of hot cracks confirms that the heat input remains moderate.

### *3.4. Analysis of precipitate volume fraction and mean radius via SAXS*

Fig. 9 shows the evolution of volume fraction and mean particle radius of the $\eta$ phase during the FE experiments performed at 16 kN and 22 kN. Quantitative estimation of temperature and precipitation within this interval is not straightforward due to the non-linear dissolution kinetics under severe plastic deformation. Since interpolation would rely on unverifiable assumptions regarding diffusion and thermo-mechanical coupling, only the measured data is presented to avoid speculation. The process can be segregated into the following stages:

**(a) Processing (Growth + Partial Dissolution):** During the processing phase of FE, where the temperature is relatively high, precipitates grow due to enhanced diffusion. However, simultaneous partial dissolution of smaller or less stable precipitates occurs, leading to a decrease in the overall volume fraction despite the increase in mean radius. This trend is also evident from the $\eta$ phase (201) peak in Fig. 6c, where a decrease in WAXS intensity is observed, consistent with the reduction indicated by the SAXS results.

(b) **Early cooling stage (nucleation+growth):** As cooling begins, the matrix becomes supersaturated while the temperature is still sufficiently high for diffusion to remain active. Smaller precipitates nucleate while the existing ones continue to grow, resulting in an increase in mean radius and a continuous increase in volume fraction. The competition between newly formed fine precipitates and the ongoing growth of the larger ones is probably reflected in a minor drop in the mean radius at the end of the early cooling stage before reaching equilibrium.

**(c) Later cooling stage (Stabilization):** At temperatures below 50 °C, there is only little diffusion. Coarsening becomes minimal, and the microstructural evolution slows down as the system becomes kinetically stabilized. The volume fraction and mean radius are almost constant.

In Fig. 9, the evolution of the mean radius and volume fraction measured from SAXS during FE is shown alongside the temperature rise due to frictional heating, is calculated using WAXS. The initial radius is around 11 nm, in the range of the precipitate size in the base material, see Fig. 10a. During processing, the mean radius significantly increases, reaching its maximum due to a rapid increase in temperature. In between, there is a small gap with no data points, caused by signal blockage from the tool. Then comes the early cooling stage, where the temperature is still high enough to favor coarsening. However,

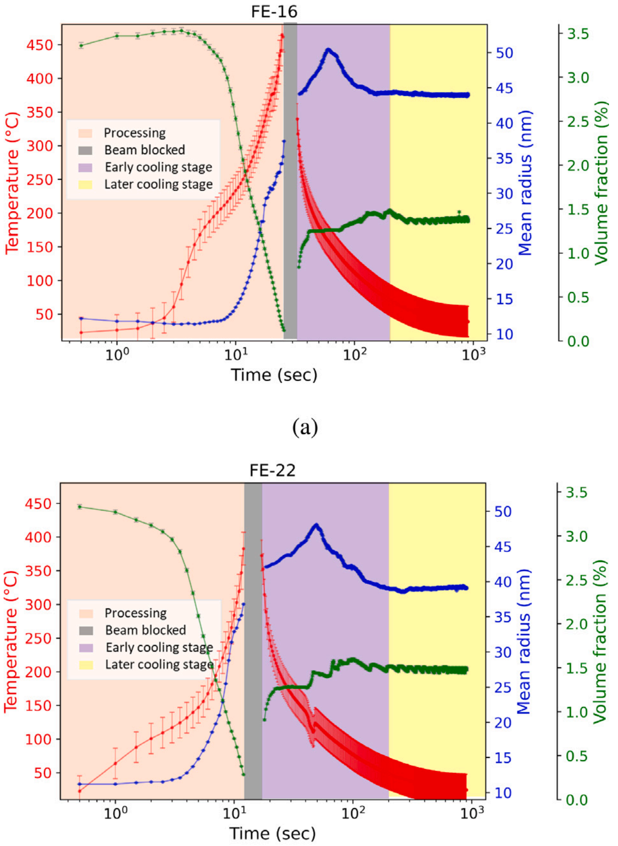

(a)

(b)

**Fig. 9.** Experimental SAXS results during the FE process showing the evolution of precipitate radius and volume fraction with increasing temperature due to frictional heating: (a) FE-16; (b) FE-22.

the temperature is decreasing as a function of time. Finally, when the temperature drops to around 100 °C, the volume fraction and mean radius become stable. Due to differences in processing time and force, the radius and volume fraction of the $\eta$ precipitates are affected significantly for both investigated process conditions.

For FE-16, more precipitate growth is observed during processing compared to FE-22, clearly due to its longer processing time and the higher process temperature reached. During the cooling stage, FE-22 results in a lower mean precipitate radius compared to FE-16. This suggests that FE-22 retains more nuclei in the form of undissolved precipitates compared to FE-16, which aligns with its shorter processing time and lower peak temperature of around 370 ± 24 °C before the beam signal is blocked. In contrast, FE-16 reaches a higher processing temperature of about 460 ± 22 °C with a longer processing time. The evolution of the critical radius is primarily governed by the solute content in the matrix. The critical radius refers to the minimum size a precipitate nucleus must reach to become stable and continue growing, and it is strongly influenced by solute concentration and temperature [38]. Since FE-22 undergoes less dissolution, it results in lower solute content in the matrix and thus a larger critical radius. In comparison, FE-16, having more solute in the matrix due to larger dissolution, exhibits a smaller critical radius, promoting faster precipitate growth and a higher mean radius. For FE-22, the precipitate mean radius was 38 ± 0.0049 nm while for FE-16 the size was 43 ± 0.0042 nm. In terms of volume fraction, for FE-16, a higher degree of precipitate dissolution is observed during processing, consistent with its higher process temperature. In the early cooling stage, an increase in volume fraction is observed for both cases. However, in FE-22, more nucleation sites are retained since fewer precipitates were dissolved during processing, leading to a higher final volume fraction compared to FE-16. In the later cooling stage, the volume fraction stabilizes as the system reaches equilibrium. For FE-16, a volume fraction of 1.3 ± 0.0001% was determined, while for FE-22 a volume fraction of 1.5 ± 0.0001% was observed. Overall, the FE-22 process tends to retain a larger volume fraction of smaller precipitates.

### 3.5. *Analysis of precipitates via STEM*

Fig. 10 shows the bright-field STEM micrographs and the selected area diffraction (SAED) pattern of the base material, FE-16, and FE-22. The microstructure reveals a homogeneous precipitate distribution. According to the literature [25], $\eta$ and $\eta'$ are the dominant phases, both exhibiting a plate-like morphology. In the SAED pattern along <112> zone axis in the BM, two streaks at 1/3 {220} and 2/3 {200} positions along {111} direction confirmed the existence of $\eta'$ precipitate [39]. After FE, both FE-16 and FE-22 exhibit a lower precipitate density and a larger mean radius compared to the base material. This suggests that smaller, metastable $\eta'$ precipitates have been dissolved during FE. The SAED patterns from the <110> zone axis show no indication of $\eta'$ precipitate in either FE-16 or FE-22. Instead, weak diffraction spots are observed near {111} for both samples, indicating the presence of equilibrium $\eta$ precipitate [40]. The size distribution was determined through manual image analysis of the STEM micrographs. The mean radius of the $\eta$ precipitates is 10.5 nm in the AA7075 base material, 35.5 nm in FE-16, and 34 nm in FE-22. In the base material, the precipitates were extremely small but grew and coarsened after FE. FE-16, processed at a higher temperature, exhibited slightly larger precipitate sizes than FE-22. A similar trend was observed in the SAXS analysis after cooling, where the mean radius increased to 43 nm for FE-16 and 38 nm for FE-22. The initial precipitate radius from SAXS was approximately 11 nm. Analysis of average aspect ratio using Fig. 10a resulted in a value of approximately 0.43, which is in excellent agreement with the value used in the SAXS model. This close correspondence confirms that the assumed ellipsoidal geometry with an aspect ratio of 0.4 provides a realistic representation of the precipitate morphology in the present study.

### 3.6. *Microhardness*

Fig. 11 summarizes the microhardness along the longitudinal cross section of the extruded wires. A variation of hardness along the wire and the lowest hardness at the center compared to the periphery is due to the different plastic deformation degrees along the radial direction, assuming that the temperature is nearly homogeneous along the wire radius and therefore no changes in precipitate distribution is expected. The average hardness is 149.5 ± 1.6 HV0.2 for FE-22 and 148.0 ± 1.2 HV0.2 for FE-16. Both precipitation strengthening mechanisms and grain boundary strengthening suggest that the hardness in FE-22 should be higher than that of FE-16. Tahmasbi and Masoud et al. [41] also reported that, at the same rotation speed, hardness increases with increasing force. Comparing microhardness to the base material (175 HV0.2), a decrease in the hardness due to the dissolution and coarsening of the precipitate is observed, which is typical for friction stir-based processed materials [12].

To further interpret the mechanical response, individual strengthening contributions to the yield strength [42] are discussed briefly in the following. The grain sizes are nearly identical (3.2 μm for FE-22 and 3.3 μm for FE-16). The calculated grain boundary strengthening based on Hall-Petch relations [42] are approximately 38.3 MPa for FE-22 and 37.7 MPa for FE-16. This marginal variation confirms that grain boundary strengthening is not the primary factor governing

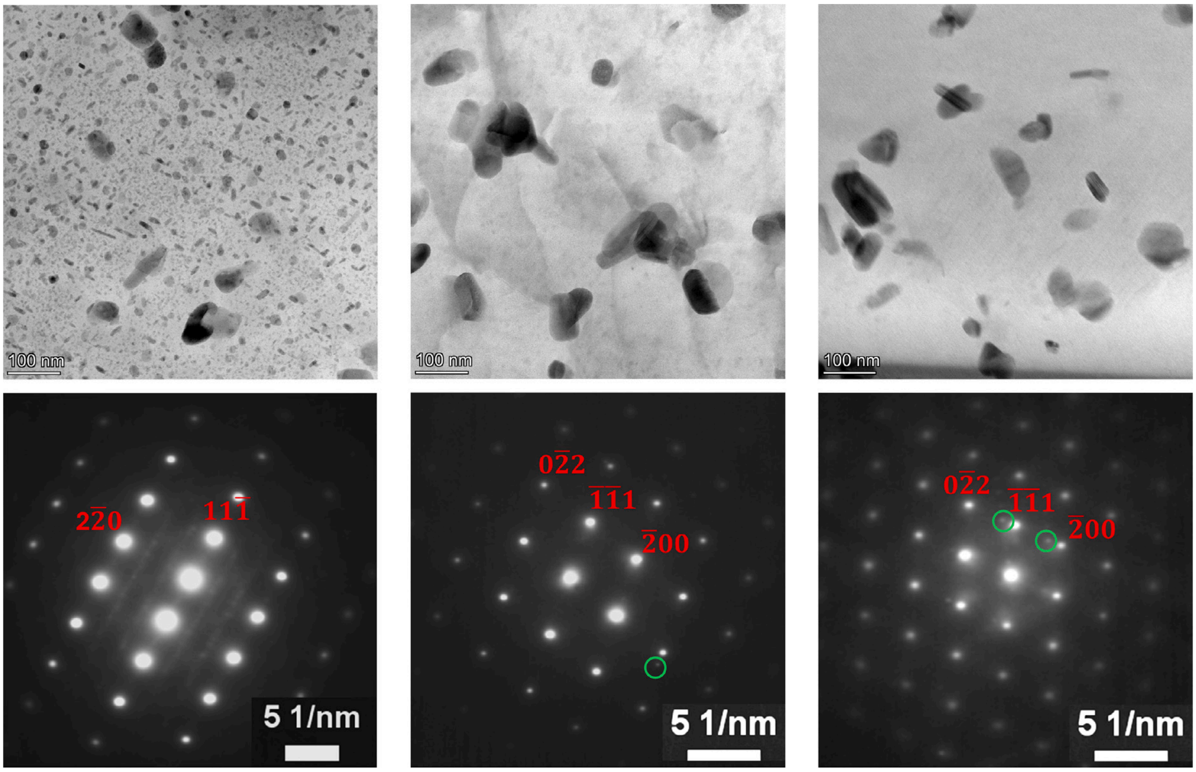

(a) (b) (c)

**Fig. 10.** Bright field scanning transmission electron microscopy (STEM) micrographs and selected area diffraction (SAED) patterns: (a) Base material AA7075-T651; (b) FE-16; (c) FE-22. The SAED patterns are captured from <112> zone axis for base material and <110> zone axis for FE-16 and FE-22. The streaks at 1/3 and 2/3 of {$2\bar{2}0$} along {111} direction indicate $\eta'$ precipitate. The corresponding diffraction spots for $\eta$ are marked in light green in FE-16 and FE-22. The mean radius of precipitates is 10.5 nm for the AA7075 base material, 35.5 nm for FE-16, and 34 nm for FE-22. (For interpretation of the references to color in this figure legend, the reader is referred to the web version of this article.)

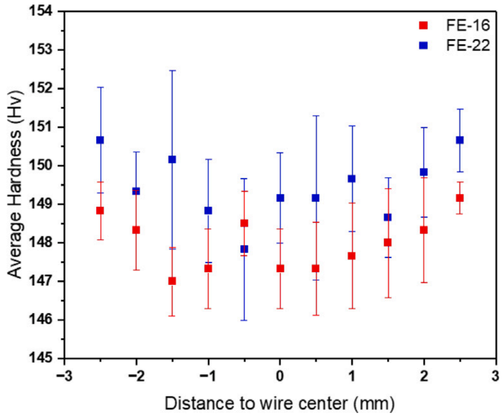

**Fig. 11.** The microhardness along the longitudinal cross section of the extruded wire for FE-16 and FE-22.

the seen hardness difference between the two conditions. In contrast, the precipitate characteristics differ more substantially: FE-16 shows a larger average precipitate radius (43 nm compared to 38 nm in FE-22) and a slightly lower volume fraction (1.3% vs. 1.5%). According to Orowan-type strengthening [42], larger particle size and reduced volume fraction increase interparticle spacing and thereby reduce precipitation strengthening.

Although additional strengthening contributions such as Mg-Cu clusters, dislocation density, solid solution strengthening, and intrinsic lattice resistance may also play a role [43], the comparable grain size suggests that the observed hardness difference is primarily governed by precipitation effects. Therefore, the slightly lower hardness in FE-16 can be attributed mainly to reduced precipitation strengthening, indicating that precipitate evolution dominates the final strength response under the present processing conditions.

## 4. Key mechanisms governing precipitation kinetics and grain refinement in friction extrusion

### 4.1. Effect of force on heat generation and temperature

Rotation combined with axial force generates frictional heat at the die-material and container-material interfaces, a mechanism well established in friction-based processes [44]. In this study, the rotation speed was kept constant, and only the applied force was varied to isolate its influence on precipitation kinetics. The higher force condition (FE-22) resulted in a shorter processing duration and a lower measured temperature in the region where the SAXS/WAXS measurements were taken, see Fig. 7. Although higher axial force can increase heat generation, in the present setup the substantially shorter processing time of FE-22 limits heat accumulation at the window side, leading to a lower local temperature. This interpretation is consistent with the observations of Li et al. [45], who reported that longer FE durations lead to higher local temperatures at comparable depths. Numerical work by Zhang et al. [44] similarly shows that localized energy dissipation at the die-material interface is a dominant contributor to temperature rise during FE.

In the current FE setup, Fig. 12, the total mechanical energy input to the process consists of the work performed by the axial extrusion force ($W^f$) and the work associated with die rotation ($W^r$). The axial work was derived from the force–displacement response over a 13 mm

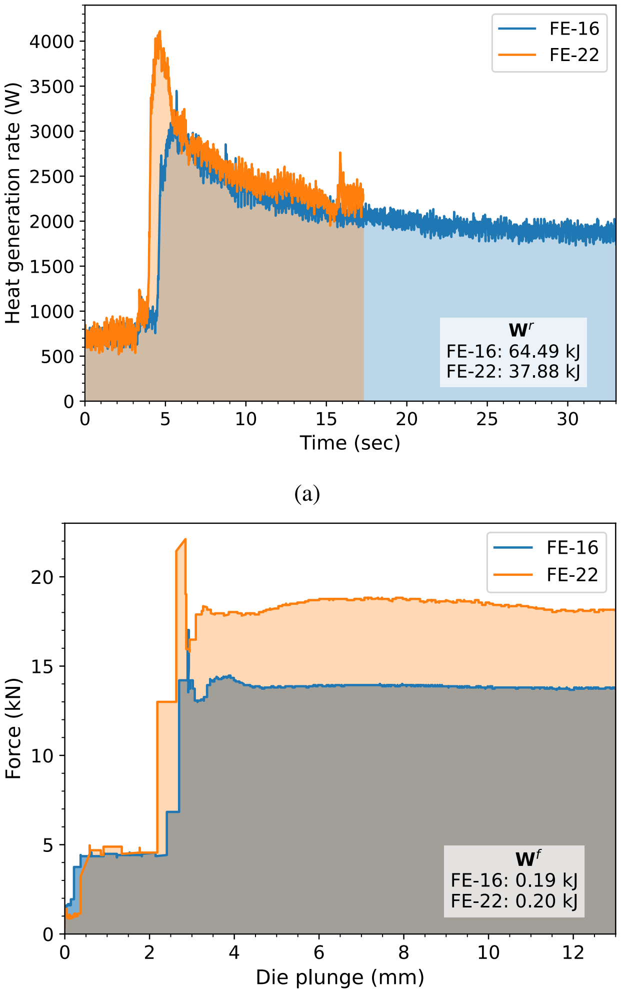

(a)

(b)

**Fig. 12.** (a) Measured die rotational power as a function of time, representing the energy input due to die rotation ($W^r$), and (b) Force as a function of die Plunge, representing energy input due to axial force ($W^f$).

die plunge, while the rotational energy was calculated by integrating the die power over the process duration. The resulting total work was 38.1 kJ for FE-22 and 64.7 kJ for FE-16. Because the FE-22 condition proceeds over a shorter time, the cumulative mechanical energy delivered to the material is lower than in FE-16, despite the higher instantaneous force and power levels. This reduced total energy input explains the lower temperature rise measured at the window region for FE-22. This interpretation is supported by the temperature obtained both from WAXS and the thermocouple placed at the window, see Fig. 7. By contrast, the die temperature remains similar for both processing conditions due to direct thermal contact with the die. It is important to note that the measured temperature reflects only the local environment at the window or die interface and does not capture the full temperature distribution in the deforming material. Spatially heterogeneous heating is expected in FE, and hotter regions may exist in zones not sampled by the thermocouple or WAXS measurement volume. The WAXS derived temperature provides an average temperature over the illuminated region, but there is currently no direct experimental method to map the complete temperature field during FE.

Frictional heat, however, depends not only on axial force and rotation but also on the interface condition. Whether the interface is in sliding or sticking contact strongly influences the amount of frictional heat and heat due to plastic deformation. Small changes in interface condition with applied force may therefore contribute to the observed temperature differences. To better interpret these effects, an analytical heat generation rate model, originally developed by Schmidt et al. [46] for FSW, is being adapted for the present FE configuration.

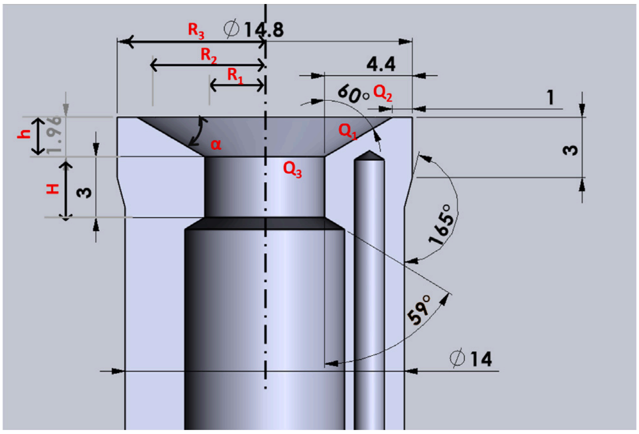

**Fig. 13.** Schematic illustration of the die tip geometry of FE setup used to calculate the heat generation rate during friction extrusion, highlighting the distinct contributions $Q_1$, $Q_2$, and $Q_3$ associated with different regions of die-material contact regions. All dimensions in mm.

### 4.2. Analytical model for heat generation rate

Similar to the analytical framework proposed by Schmidt et al. [46], the present model assumes axisymmetric contact between the rotating die and the deforming material, with uniform contact shear stress distributed over the entire contact area. This formulation implicitly assumes a constant effective friction coefficient and a spatially averaged contact pressure in accordance with Coulomb's friction law [47]. The die is considered rigid, and the angular velocity is taken as constant during each evaluated time interval. Furthermore, heat generation is assumed to originate primarily from interfacial friction, while local variations in temperature, pressure, sliding velocity, and material flow are not explicitly resolved.

While local variations in temperature, pressure, and sliding velocity exist, this approximation enables a closed-form analytical estimate of frictional heat generation and provides an upper-bound assessment. It is important to note that, unlike FSW, FE does not represent a fully steady-state process, as the contact conditions, extrusion force, and material flow evolve continuously with time. However, during the final stage of the process, the extrusion force becomes approximately constant, see Fig. 7, indicating a locally quasi-steady operating regime. Consequently, the analytical framework is applied here in a qualitative and comparative sense to interpret transient force and contact condition relationships over limited time intervals, where the process may be considered locally quasi-steady. This approach enables insight into the prevailing contact condition without assuming global steady-state behavior.

Three different analytical estimates are utilized in terms of contact conditions, with an overall assumption of uniform contact shear. Firstly, a sticking interface condition ($\delta = 1$) is assumed. Secondly, a pure sliding condition ($\delta = 0$) is employed, which is described by the Coulomb interaction. Finally, a partial sliding/sticking condition estimate is utilized. During FE, the heat is generated where the die is in contact with the material, see Fig. 13. A 60° die angle was employed; the contact angle, $\alpha$, with the material is 30°. The heat generated is seggregated in three parts:

**(a) Heat generation rate under the die with conical surface ($Q_1$):** The die angle was conical in shape. The final heat generated in this region from radius $R_1 = 3$ mm to $R_2 = 6.40$ mm can be calculated by integrating the following equation:

$$Q_1 = \int_0^{2\pi}\int_{R_1}^{R_2} \omega\tau_{contact} r^2[1 + tan\ \alpha]dr\ d\theta = \frac{2\pi}{3}\omega\tau_{contact}(R_2^3 - R_1^3)(1 + tan\ \alpha), \quad (1)$$

where $\omega$ is the tool angular rotational speed and $\tau_{contact}$ is the shear contact stress.

**(b) Heat generation rate under the die with flat surface** ($Q_2$)**:** The final heat generated in this region from $R_2 = 6.40$ mm to $R_3 = 7.40$ mm can be calculated by integrating the following equation:

$$Q_2 = \int_0^{2\pi}\int_{R_2}^{R_3} \omega\tau_{contact} r^2 dr\ d\theta = \frac{2\pi}{3}\omega\tau_{contact}(R_3^3 - R_2^3), \quad (2)$$

**(c) Heat generation rate after the die orifice** ($Q_3$)**:** The die has a cylinder surface at the die orifice with a height $H$ of 3 mm. Afterwards, the radius is increased from 3 mm to 4 mm, assuming no contact of the extruded wire with the wall anymore. Therefore, after integrating the total heat generated in this region results in:

$$Q_3 = \int_0^{2\pi}\int_0^{H} \omega\tau_{contact} R_1^2 dh\ d\theta = 2\pi\omega\tau_{contact} R_1^2 H. \quad (3)$$

The total heat generation rate is determined from all three contributions combined which can be simplified as follows:

$$Q_{total} = Q_1 + Q_2 + Q_3 = \frac{2}{3}\pi\omega\tau_{contact}[(R_2^3 - R_1^3)(1 + tan\ \alpha) + (R_3^3 - R_2^3) + 3R_1^2 H]. \quad (4)$$

### 4.2.1. *Heat generation ratio*

Independent of the actual contact conditions, the contributions from the different surfaces is compared to the total heat generated:

$$\frac{Q_1}{Q_{total}} = \frac{(R_2^3 - R_1^3)(1 + tan\ \alpha)}{(R_2^3 - R_1^3)(1 + tan\ \alpha) + (R_3^3 - R_2^3) + 3R_1^2 H} = 0.62$$

$$\frac{Q_2}{Q_{total}} = \frac{(R_3^3 - R_2^3)}{(R_2^3 - R_1^3)(1 + tan\ \alpha) + (R_3^3 - R_2^3) + 3R_1^2 H} = 0.24 \quad (5)$$

$$\frac{Q_3}{Q_{total}} = \frac{3R_1^2 H}{(R_2^3 - R_1^3)(1 + tan\ \alpha) + (R_3^3 - R_2^3) + 3R_1^2 H} = 0.14$$

This indicates that for the present FE tool geometry, the majority of heat generation (86%) comes from the region in front of the die orifice. Moreover, the conical surface contributes more to heat generation compared to the flatter surface, while the region after the die orifice accounts for only 14% of the total heat.

### 4.2.2. *Comparison of analytical and experimental heat generation rate of the die for FE-16 and FE-22*

The input parameters used in the analytical model are listed in Table 4. Each analytical estimate corresponds to a specific contact condition, which directly influences the assumed contact shear stress and, consequently, the calculated heat generation rate. For details of the governing equations and underlying approximations, refer to Schmidt et al. [46].

**(a) Sticking condition** ($\delta = 0$)**:** Under the sticking condition, where $\tau_{contact} = \sigma_{yield}/\sqrt{(3)}$ holds, the effective yield strength at processing temperature for both processes, FE-16 and FE-22, is determined via:

$$\sigma_{yield} = \frac{3\sqrt{3}Q_{total}^{sticking}}{2\pi\omega[(R_2^3 - R_1^3)(1 + tan\ \alpha)(R_3^3 - R_2^3) + 3R_1^2 H]}. \quad (6)$$

**Table 4**
Input parameters of analytical heat generation model. The frictional coefficient, $\mu$ is taken from Ref. [47].

| Input parameter | Unit | Value |
|---|---|---|
| $R_1$ | mm | 3 |
| $R_2$ | mm | 6.4 |
| $R_3$ | mm | 7.4 |
| $H$ | mm | 3 |
| $h$ | mm | 1.96 |
| $\omega$ | rad/s | 31.42 |
| $\mu$ | – | 0.5 |

**Table 5**
Process and the calculated yield strength when we assume sticking conditions.

| Process name | Exp. heat generation rate [W] | Calculated yield strength [MPa] |
|---|---|---|
| FE-16 | 1900.5 | 84.1 |
| FE-22 | 2291.8 | 101.4 |

The heat generation rate of the die is known and directly taken from the monitored values at the end of the experiments when the process reaches a quasi-steady operating regime. Table 5 shows the heat generation rate of the die, calculated yield strength for both the processes under the ideal case of completely sticking contact condition. The experimental value of yield strength for AA7075 at a temperature around 400 °C is reported to be less than 100 MPa [48,49]. In the current case, the values are determined to be in the range of 80–100 MPa, see Table 5, which is higher than reported values during quasi-static tensile testing. The determined value in the current cases is affected by strain rate and pressure effects, leading to a significant higher equilibrium yield strength compared to its quasi-static values, which is consistent with observations by Reimann [50] for refill FSSW.

**(b) Sliding condition** ($\delta = 1$)**:**

Under sliding conditions, the total heat generation rate is calculated using Eq. (8), which is derived from Eq. (4). According to Coulomb's friction law, the contact shear stress is given by $\tau_{\text{contact}} = \mu p$, where the contact pressure is defined as $p = F_{\text{exp}}/A_{\text{contact}}$. Here, $F_{\text{exp}}$ denotes the experimentally measured plunge force, and the contact area is expressed as:

$$A_{\text{contact}} = \pi[(R_3^2 - R_2^2) + (R_2 + R_1)l], \quad (7)$$

where $l$ is the lateral length of the truncated cone, given by $l = \sqrt{h^2 + (R_2 - R_1)^2}$, and $h$ is the height of the truncated cone. The experimentally measured force is used as input to the analytical model to evaluate the corresponding sliding power as follows:

$$Q_{total}^{sliding} = \frac{2}{3}\mu\omega\frac{F_{exp}}{[(R_3^2 - R_2^2) + (R_2 + R_1)l]} \times [(R_2^3 - R_1^3)(1 + tan\ \alpha) + (R_3^3 - R_2^3) + 3R_1^2 H]. \quad (8)$$

The resulting heat generation rates under both sticking and sliding assumptions are compared with experimental measurements in Fig. 14 for FE-16 and FE-22. The analytical predictions obtained under the ideal condition of sliding contact show good agreement with the experimentally measured heat generation rate during the stage of the process where the plunge force becomes approximately constant. Furthermore, the predicted heat generation rate under sliding conditions follows the experimentally measured torque evolution, confirming the proportional relationship $Q = T\omega$ during the quasi-steady stage. During this stage, the measured torque is approximately 60 N m for FE-16 and 70 N m for FE-22, while the analytical model predicts torques of 60.5 N m and 72.9 N m for FE-16 and FE-22, respectively. In contrast, the sticking condition represents an upper bound for the heat generation rate.

**(c) Partial sticking and sliding** ($0 < \delta < 1$)**:**

To assess whether sliding or sticking dominates the die-material contact condition, the proportionality between the experimentally measured plunge force and the heat generation rate is examined, following

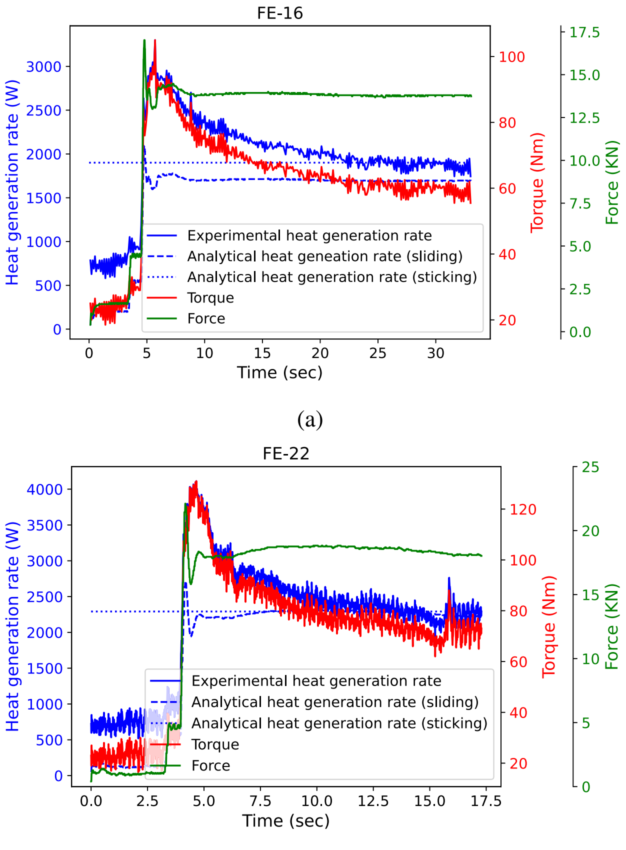

(a)

(b)

**Fig. 14.** Comparison of experimentally measured and analytically estimated die heat generation rates for (a) FE-16 and (b) FE-22. The plots show the temporal evolution of the measured plunge force and torque together with the corresponding analytical heat generation rates calculated under sliding and sticking contact assumptions. The analytical sliding solution is based on the experimentally measured force input, while the sticking solution represents an upper bound for the heat generation rate.

**Table 6**
Ratio of heat generation rate to applied force within the proportional region.

| Process name | Mean ratio | 95% Confidence interval |
|---|---|---|
| FE-16 | 0.138 ± 0.004 | [0.1381, 0.1386] |
| FE-22 | 0.126 ± 0.006 | [0.1245, 0.1265] |

the approach proposed by Schmidt et al. [46]. In their model, the absence of proportionality between force and heat generation rate suggested a predominantly sticking contact condition. However, for the FE-16 case, there is a clear proportional relationship between force and heat generation after approximately 22 s, suggesting that FE-16 operates closer to a sliding contact condition during this period. In contrast, for the FE-22 case, proportionality between force, torque, and power is observed only near the end of the process (around 16 s), indicating that even at higher force levels, the process exhibits some sliding behavior. However, the trend suggests that higher forces tend to correspond to increased sticking or reduced sliding contact, which is in agreement with experimental observations in the literature [13]. To quantify this relationship, the ratio of heat generation rate to applied force was calculated within the proportional region (after 22 s and 16 s for FE-16 and FE-22, respectively), as shown in Table 6. The stability of this ratio suggests a proportional relationship between force and heat generation, consistent with sliding contact conditions [46].

Microstructurally, the presence of sliding conditions is supported by the observation of more refined grains in the edge and elongated grain sizes in the wire center, see Fig. 8. These features are consistent with literature reports distinguishing sliding and sticking friction regimes in friction extrusion processes [13].

### 4.3. *Effect of strain and strain rate on precipitation kinetics*

The severe deformation imposed during FE is expected to strongly influence precipitation kinetics, primarily through the action of dislocations generated during plastic straining. These dislocations act as highly efficient heterogeneous nucleation sites and create fast-diffusion pathways through pipe diffusion, thereby accelerating both nucleation and growth when deformation and precipitation occur simultaneously [51]. More broadly, according to Deschamps et al. [52], when deformation and precipitation proceed simultaneously, the interaction is complex and highly dynamic. Elastic stresses may influence variant selection for precipitates that possess significant lattice mismatch with the matrix. The effects of plastic strain is governed by several mechanisms: dislocations can enhance nucleation; pipe diffusion and dislocation sweeping can accelerate growth and coarsening; deformation-generated excess vacancies may further promote nucleation and growth; and, in some cases, precipitates may be sheared and partially or fully dissolved. Depending on which of these competing mechanisms dominates under given conditions, a wide range of behaviors has been observed experimentally, from accelerated nucleation, to rapid growth and coarsening, to strain-induced dissolution. The balance among these mechanisms is governed by supersaturation, temperature, and precipitate morphology, as well as by the imposed strain magnitude, strain rate, and deformation temperature [52].

Due to limited azimuthal coverage of the diffraction ring, reconstruction of the full strain tensor was impossible for FE-16 and FE-22, respectively. However, directional elastic strain due to load obtained from WAXS measurements (Appendix C) confirms that the material experiences significant deformation during the extrusion process. Several studies [51] have shown that even modest plastic strains can significantly modify the precipitation response of Al alloys. A useful benchmark is the in-situ SAXS investigation by Deschamps et al. [52], where a 7xxxx series alloy strained to only 0.06 plastic strain at a strain rate of 6 x $10^{-5}$ $s^{-1}$ at 160 °C exhibited a 50% increase in precipitate size within 30 min relative to an unstrained specimen subjected to the same thermal profile. Although the thermo-mechanical conditions during FE involve far higher strain rates ($\approx 3$–$100$ $s^{-1}$ [53,54]) and much larger strains ($\approx 3-10$) [14,45], this comparison illustrates that even incremental plastic strains can dramatically enhance nucleation and growth kinetics. In this context, the simultaneous strain assisted precipitate growth observed in FE-16 and FE-22, even while some dissolution occurs due to rising temperature in the SAXS/WAXS measurement zone, is consistent with the expected acceleration of precipitation processes in the presence of deformation, which is inhomogeneous across the measured region.

Finally, both SAXS and TEM results indicate a more than 4 times increase in average precipitate size after FE. This dramatic growth is attributed to the combined effect of severe plastic deformation and elevated temperature.

### 4.4. *Recrystallization and grain size evolution*

Next, the distinct microstructural evolution and transition behavior within extruded wires is evaluated via EBSD analysis at the center and edge regions of the base material (BM) and FE-16 extruded wire. The FE-22 extrudate exhibits a slightly different grain size compared to the FE-16 extrudate; however, the grain morphology and the underlying dynamic recrystallization mechanisms share a high similarity. For brevity, the FE-22 results are included in Appendix D. Fig. 15 summarizes the inverse pole figures (IPF), corresponding (111) and (110) pole figures (PFs), texture intensities (expressed in multiples of random distribution, mrd), average grain sizes (AGS) and GOS maps.

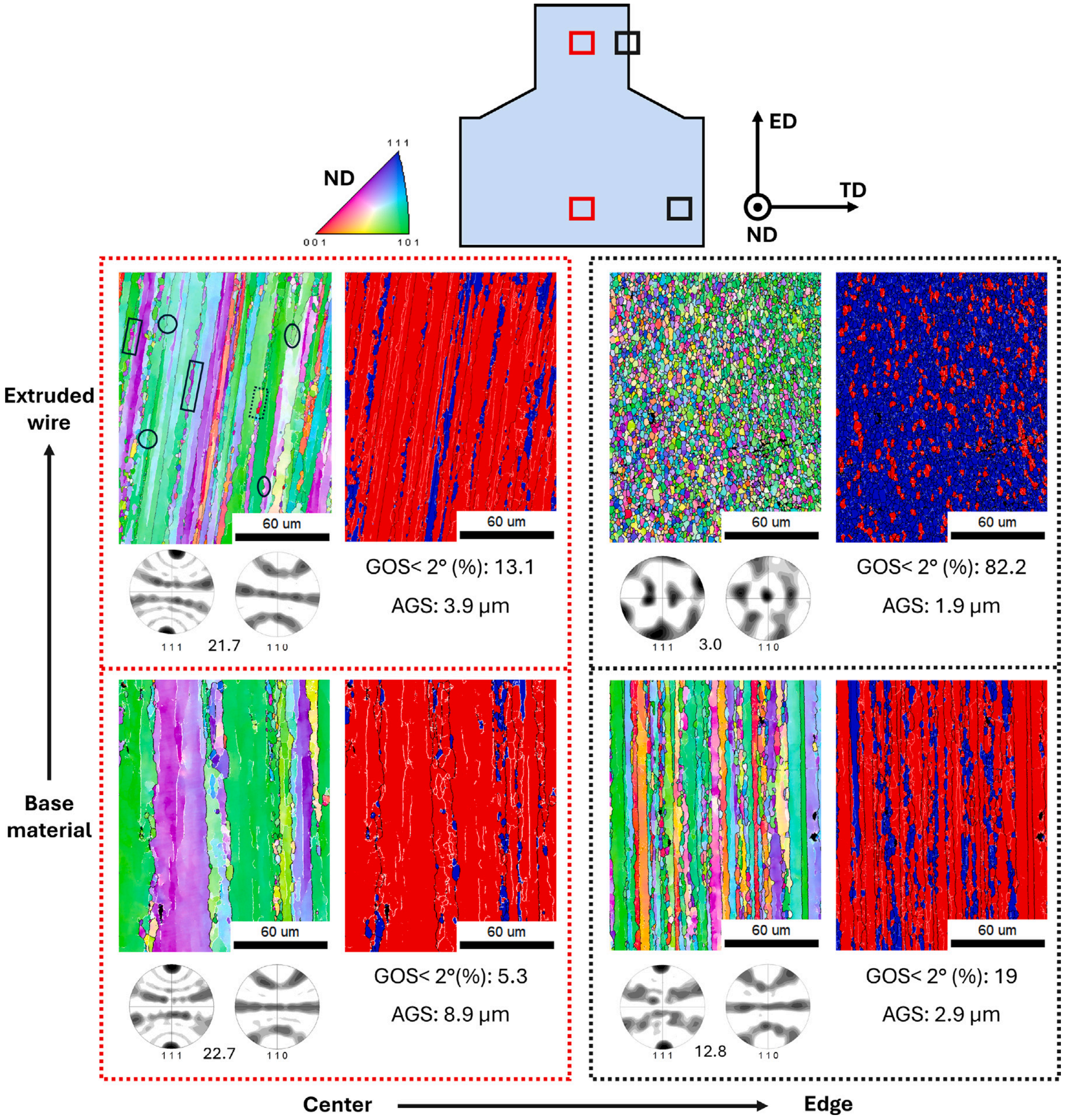

**Fig. 15.** Electron backscatter diffraction (EBSD) microstructural characterization of the base material and the extruded wire at 16 kN. Inverse pole figure (IPF) maps are shown for both the center and the edge regions of the specimens. The corresponding pole figures illustrate the texture evolution with the intensities in multiples of random distribution (mrd). The degree of recrystallization is represented in the fraction of grain orientation spread (GOS) <2° and the average grain size was assessed by the high-angle grain boundaries (HAGBs) spacing perpendicular to extrusion direction (ED).

The AGS is calculated by HAGBs spacing perpendicular to extrusion direction (ED) due to the morphology of the grains. The BM exhibits a typical grain morphology of extruded Al alloys, characterized by elongated grains aligned with the ED. PFs depict a strong <111> fiber texture along the ED, resulting from the alignment of primary slip systems during deformation in Al alloys [55]. Within BM, a notable grain size gradient is present. The AGS at the edge (2.9 µm) is significantly smaller than at the center (8.9 µm). This initial gradient is attributed to higher friction between the die orifice and the extrudate during the BM manufacturing, which facilitates dynamic recrystallization (DRX) [56]. The center of the extruded wire remains a similar morphology as in the BM, consisting of elongated grains decorated with few finer grains (AGS of 3.9 µm). This moderate grain refinement is driven mainly by the extrusion ratio accompanying occasional DRX as evidenced by a minor increase in the fraction of grains with GOS <2°. Notably, at the center of the extruded wire, the characteristic extrusion texture deviates clockwise from the ED. This shift is due to the geometrical effect of strain, indicating the minor influence of the rotational motion during processing. In contrast, the edge of the FE-16 extruded wire is composed predominantly of fine grains (AGS of 1.9 µm). The high degree of DRX in this region is confirmed by the GOS distribution, where over 82% of the grains exhibit values <2°.

The degree of DRX is directly manifested in the texture intensity. Within the BM, a significant reduction in texture intensity is observed from the center (22.7 mrd) to the edge (12.8 mrd), where the fraction of GOS <2° increases from 5.3 to 19%. This inverse relationship between DRX degree and the texture intensity is also evident in the extruded wire, where the intensity drops from the center (21.7 mrd) to the edge (3 mrd) and the fraction of GOS <2° increases from 13.1 to 82.2%. Notably, the characteristic extrusion texture is preserved at the extruded wire center, while a texture alternation at the edge of the extruded wire is observed. This transition is attributed to severe plastic

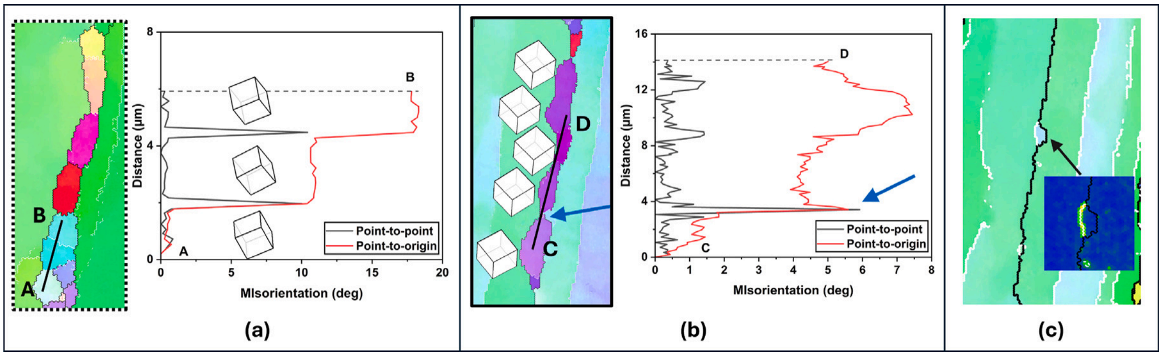

**Fig. 16.** Misorientation distribution along elongated grains, see Fig. 15, with (a) and without (b) sub-grain rotation. (c) Grain boundary bulging at the existing HAGBs due to boundary migration and corresponding kernel average orientation (KAM) map.

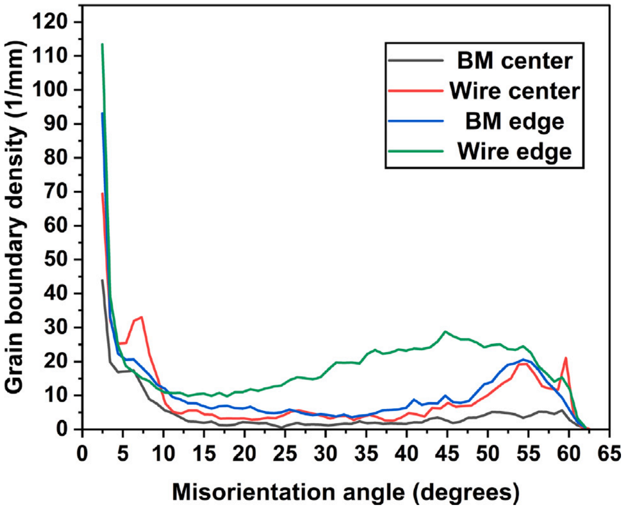

**Fig. 17.** Evolution of grain boundary densities at the center and edge regions of the base material (BM) and the extruded wire taken from the identified regions in Fig. 15.

deformation coupled with the high temperature exposure, initiating intensive DRX. These findings align well with the literature, indicating that the extruded wire center experienced lower plastic strain and the extrusion-induced shear is the dominant deformation mode [13]. In contrast, the extruded wire edge experienced significantly higher plastic strain, dominated by shearing. Microstructural analysis revealed evidence of multiple DRX mechanisms. Continuous dynamic recrystallization (CDRX) and geometrical dynamic recrystallization (GDRX) are commonly reported in Al alloys [57]. While certain elongated grains exhibit clear evidence of sub-grain rotation, Fig. 16a, it is absent in others, Fig. 16b. The former is characterized as CDRX and the latter as GDRX [57]. It is worth noting that one end of the elongated grain shown in Fig. 16b is nearly forming a new refined grain (indicated by the red arrow). This morphology is hypothesized to represent the microstructural state immediately prior to the pinch off, which results in forming refined, equiaxed grains. In addition to CDRX and GDRX, grain boundary bulging (indicated by black circles in Figs. 15 and 16c was observed extensively at the extruded wire center, which might imply the occurrence of DDRX. The kernel average misorientation (KAM) map in Fig. 16c shows a high KAM value at the concave side of the bulging, implying a strain induced subboundary [57]. While the occurrence of DDRX in high stacking fault metals like Al remains in debate, it has been frequently documented in friction stir based processes [58].

To evaluate the evolution of grain boundaries from the BM to the extruded wire, the misorientation angle distribution was analyzed in terms of grain boundary density, calculated by the total boundary length normalized by the EBSD scan area. Fig. 17 illustrates these distributions for the region identified in Fig. 15, while Table 7 summarizes the absolute values and the percentage increase for both low angle grain boundaries (LAGBs) and high angle grain boundaries (HAGBs). Upon passing through the die orifice, all regions exhibit an increase in both LAGB and HAGB densities, marking the formation of deformation-induced grain boundaries. However, the behaviors differ significantly between the center and edge regions. At the center region, a bimodal distribution is present, with density peaks occurring at approximately 5–8° and 50–60°. The sharp increase in high misorientation angles is reported to be associated with GDRX [59] and potentially DDRX. Additionally, the misorientation angles range between 10–40° shows minimal growth. This suggests that the transition from LAGBs to HAGBs due to dislocation accumulation induced by deformation is minimum, indicating limited CDRX in this region. In contrast, the edge of the extruded wire exhibits no bimodal distribution. Instead, it displays a uniform increase across the misorientation angle distribution, with the major gains occurring at angles higher than 30°. This trend suggests a high degree of dislocation accumulation and subsequent transformation from LAGBs to HAGBs. Therefore, the grain refinement observed from BM to the extruded wire should be determined mainly driven by GDRX and CDRX, where GDRX is more pronounced at the center region and accompanied by DDRX [57], and the CDRX is more pronounced at the edge due to the higher experienced strain [60]. The interplay between strain rate, $\dot{\varepsilon}$, and temperature on dynamic recrystallization is usually described through Zener-Holloman equation, $Z = \dot{\varepsilon} \cdot e^{\frac{Q}{RT}}$, where $Q$ is the materials' activation energy, and $R$ is the universal gas constant. The Z value is proportional to the strain rate and inversely proportional to the temperature. With the large deviation of strain rate in the literature [53], it is hard to conclude the influence of processing force on the DRX degree. The effect of the Z value on the DRX mechanisms remains controversial in the literature. Some studies have shown that a higher Z value favors CDRX in the thermo-mechanical processing of Al alloys [59], whereas others have claimed that DDRX is favored at a higher Z value [61]. However, from the analytical calculation, FE-22 tends to increase the sticking contact, implying that more shear strain is introduced into the system at higher force, and thus a slightly higher degree of DRX is expected. Additionally, the lower processing temperature hinders grain growth in FE-22, which also leads to a smaller grain size.

## 5. Summary

This study presents an in-situ investigation of friction extrusion performed using the FlexiStir system at a high-energy synchrotron beamline. In combination with wide and small angle X-ray scattering measurements, the temperature and dynamic precipitate evolution during the friction extrusion of AA7075 were determined. This approach

**Table 7**
Grain boundary density (1/mm) and high angle grain boundaries fraction ($f_{HAGB}$) at center and edge of the base material (BM) and extruded wire as well as the increase in low angle grain boundaries (LAGBs), HAGBs and all grain boundaries.

| | | Grain boundary density (1/mm) | | | $f_{HAGB}$ |
|---|---|---|---|---|---|
| | | LAGBs | HAGBs | All | |
| Center | Base material | 166.3 | 122.8 | 289.1 | 42.5 |
| | Extruded wire | 262.1 | 274.9 | 537.0 | 51.2 |
| | Trend | +58% | +124% | +86% | |
| Edge | Base material | 289.6 | 396.1 | 685.7 | 57.8 |
| | Extruded wire | 317.4 | 902.0 | 1219.4 | 74 |
| | Trend | +10% | +128% | +78% | |

enables characterization of microstructural evolution under the coupled thermal and mechanical conditions that occur during friction extrusion.

During processing, a decrease in the intensity of the $\eta$ precipitate (201) peak was observed, indicating partial dissolution. However, peaks corresponding to the $\eta$ precipitate still remained after processing, implying that the $\eta$ phase was not completely dissolved and remained present in the material. The FE process at a lower applied force (FE-16), which lasted for a longer duration, resulted in higher temperatures. Temperature was directly calculated from the lattice expansion measured over time and compared with thermocouples placed near the window and die. To understand the effect of force on temperature, the total mechanical work input from die rotation and axial force was evaluated. The analysis highlights a fundamental relation between the process and temperature, showing that variations in applied force and processing duration control the thermal exposure of the material during friction extrusion. The analysis shows that the process with a shorter duration and higher applied force resulted in a lower total work input, even though a higher experimental heat generation rate was recorded. In addition, an analytical model was employed to assess frictional heating arising from the die-material interface contact condition, which is another important contributor to the temperature increase. Based on the die geometry, the majority of heat generation occurs beneath the die. Both FE-16 and FE-22 were found to operate predominantly under sliding contact conditions, demonstrating that frictional sliding plays a dominant role in heat generation during the process.

SAXS analysis revealed that the FE process at a lower force (FE-16) led to a higher mean precipitate radius but a lower volume fraction compared to the higher-force process (FE-22). This indicates that higher processing temperatures promote precipitate growth, while lower temperatures and shorter durations favor the retention of a higher number of smaller precipitates. These observations demonstrate that the precipitation kinetics during friction extrusion are strongly governed by the combined effects of temperature and strain rate, which accelerate diffusion driven precipitate coarsening under severe thermo-mechanical conditions. A lower stable volume fraction was observed for FE-16 in comparison to FE-22. This suggests that the higher force condition (FE-22) leads to a smaller mean precipitate size and a higher retained volume fraction, which is likely to enhance yield strength and hardness due to more effective precipitation strengthening. TEM analysis confirmed these observations on the precipitate size.

Macrostructural analysis confirmed that sound, defect-free wires were obtained for both FE-22 and FE-16 processing conditions. Microstructural characterization further reveals that grain refinement during friction extrusion results from a combination of dynamic recrystallization mechanisms governed by the local strain and temperature distribution. At the wire center, the preservation of elongated grain morphology and characteristic extrusion texture indicates relatively low localized plastic strain, where the grain refinement is mainly driven by GDRX accompanied by DDRX. In contrast, the wire edge undergoes homogeneous recrystallization driven by CDRX due to a higher localized plastic strain. The degree of grain refinement is influenced by the processing parameters. The higher extrusion force employed in the FE-22 sample facilitated higher shear deformation, resulting in slightly finer grain sizes compared to the FE-16 sample. Despite the grain refinement achieved during processing, the thermal cycle associated with friction extrusion promotes precipitate dissolution and coarsening, resulting in a reduction in hardness.

Overall, the presented findings establish a direct process, temperature, and microstructure linkage during friction extrusion, demonstrating how process parameters control thermal exposure, precipitation kinetics, and grain refinement under severe thermo-mechanical conditions. Beyond the specific AA7075 case, these findings highlight generic mechanisms governing precipitation evolution and recrystallization during friction-based and severe plastic deformation processes. The present in-situ approach demonstrates that time-resolved synchrotron experiments can reveal dynamic microstructural transformations during processing, enabling a deeper understanding of the coupling between deformation, temperature evolution, and phase transformations. From an engineering perspective, this provides a framework for optimizing thermo-mechanical processing routes to tailor microstructure and mechanical properties in advanced lightweight alloys. Future efforts should aim to couple such in-situ observations with thermodynamic and kinetic modeling to predict phase evolution and guide process design for next-generation lightweight structural materials. In addition, extending such experiments to different alloy systems and processing conditions would further establish general design principles for controlling precipitation and recrystallization during severe thermo-mechanical processing. Additionally, a complementary in-situ heat treatment experiment without deformation would provide valuable insight into isolated thermal effects.

## CRediT authorship contribution statement

**Elizabeth Mathew:** Writing – review & editing, Writing – original draft, Validation, Software, Methodology, Investigation, Conceptualization. **Chang Yin-Cheng Chan:** Writing – review & editing, Writing – original draft, Validation, Methodology, Investigation. **Lars Rath:** Writing – review & editing, Validation, Investigation, Conceptualization. **Julian Escobar:** Writing – review & editing, Validation, Investigation. **Emad Maawad:** Investigation. **Harikrishnasinh Rana:** Writing – review & editing, Investigation. **Uceu Fuad Hasan Suhuddin:** Writing – review & editing, Validation. **Peter Staron:** Writing – review & editing, Validation, Resources. **Jorge F. dos Santos:** Writing – review & editing, Resources. **Benjamin Klusemann:** Writing – review & editing, Supervision, Resources, Project administration, Methodology, Funding acquisition, Conceptualization.

## Funding

This project has received funding from the European Research Council (ERC) under the European Union's Horizon 2020 research and innovation programme (grant agreement No 101001567).

## Declaration of competing interest

The authors declare that they have no known competing financial interests or personal relationships that could have appeared to influence the work reported in this paper.

## Acknowledgments

We acknowledge DESY (Hamburg, Germany), a member of the Helmholtz Association HGF, for the provision of experimental facilities. Parts of this research were carried out at PETRA III. Data was collected using SAXS and WAXS at P07 operated by Helmholtz-Zentrum Hereon. Beamtime was allocated for proposal I-20230278. Additionally, the authors gratefully acknowledge Prof. Dr. Florian Pyczak and

Dr. Mark Timothy Mordridge from Helmholtz-Zentrum Hereon for their support and assistance with the TEM measurements. J.E. and J.F.S. acknowledge that part of this research was supported by the Energy Mission Seed Investment, under the Laboratory Directed Research and Development (LDRD) Program at Pacific Northwest National Laboratory (PNNL). PNNL is a multi-program national laboratory operated by Battelle Memorial Institute for the U.S. Department of Energy (DOE) under Contract No. DE-AC05-76RL01883.

## Appendix A. Sapphire glass artifacts captured using WAXS during FE

Fig. 18 shows the 2D Debye–Scherrer rings captured by WAXS towards the end of the process, showing some small sapphire glass artificats. The precipitate rings are not directly affected, and after integration, the artifact signals were not strong enough to interfere with phase identification.

## Appendix B. Temperature measurement using WAXS data

The temperature was determined by calculating the change in lattice constant as a function of time from the WAXS data.

A second-order polynomial regression was obtained from the experimental lattice constant-temperature data reported by Guèrard et al. [62], where the relative lattice parameter change ($\Delta a/a_o$) was analyzed as a function of temperature. The resulting parametric fit equation,

$$T = 22.6 + 4.14 \times 10^4 \Delta a/a_o - 4.18 \times 10^5 (\Delta a/a_o)^2 \tag{B.1}$$

with an $R^2$ value of 0.997, was used to convert the lattice constant measurements of the Al (200) peak from the WAXS signal into temperature as a function of time, see Fig. 19.

## Appendix C. Temperature measurement considering the load

FE is a severe thermo-mechanical processing technique used to extrude materials. Temperature and load during the process are critical for obtaining sound extruded wires [21].

The total strain ($\epsilon^{tot}$) obtained from the change in lattice constant consists of two components: thermal strain, $\epsilon^{th}$ (due to temperature), and elastic strain, $\epsilon^{l}$ (due to load). Therefore, the thermal strain due to load can be determined as:

$$\epsilon^{th} = \epsilon^{tot} - \epsilon^{l} \tag{C.2}$$

Previously, in-situ studies [21,63] have shown that diffraction techniques can be used to determine stress via scattering vectors measured along three orthogonal directions. In the present study, however, measurements were performed only in one direction. Therefore, no information on axial strain is available. The tangential and radial stresses cancel out during FE. Nevertheless, the applied load induces an elastic strain, $\epsilon^{l}$, in the material. This strain is estimated by first calculating the corresponding stress from the measured load and then applying Hooke's law using the Young's modulus, $E$. Since $E$ is temperature-dependent, its variation with temperature was calculated for the WAXS-derived temperatures of FE-16 and FE-22, as shown in Fig. 20a,b, respectively. Using these values of $E$ and the measured load, $\epsilon^{l}$ was calculated using Hooke's law, as shown in Fig. 20c. The results indicate that $\epsilon^{l}$ increases as the material softens, consistent with the temperature dependence of $E$. The thermal strain, $\epsilon^{th}$, was calculated according to Eq. (C.2). Fig. 20d shows the corresponding thermal strains for FE-16 and FE-22. The temperature was determined using the method described in Appendix B. The calculated temperature difference was less than 10 K.

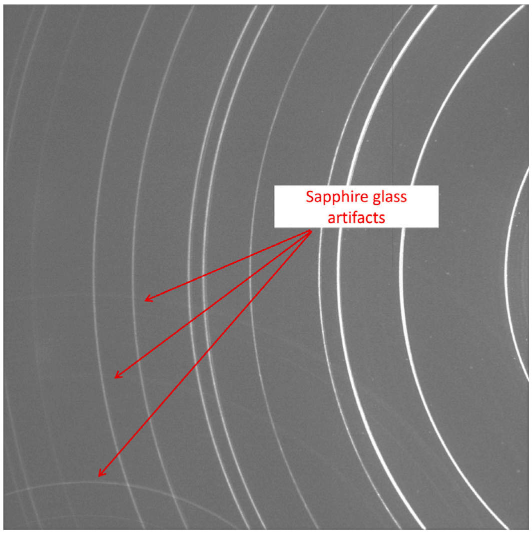

**Fig. 18.** Sapphire glass artifacts captured using WAXS during FE.

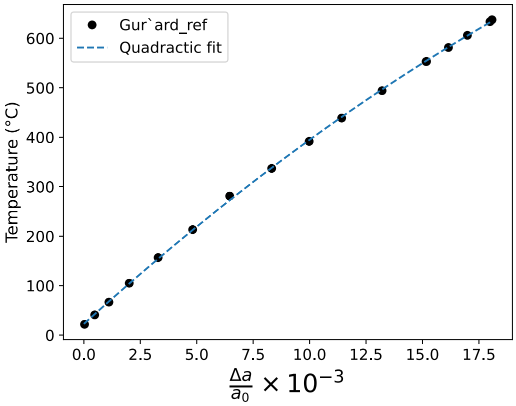

(a)

**Fig. 19.** (a) Parametric fit of temperature as a function of relative lattice constant change, Literature data from Guèrard et al. [62].

## Appendix D. Microstructural features of the FE-22

The distinct microstructural features at the center and edge of FE-22 are summarizes in Fig. 21. The average grain size at the edge is 1.7 μm and 5 μm at the center. Next, a typical extrusion texture with a texture intensity of 17.4 mrd and a simple shear texture with texture intensity of 2.4 mrd are observed at the center and the edge of the FE-22, respectively. This microstructural trend closely aligns with the FE-16 specimen. Notably, the typical extrusion texture at the center of FE-22 exhibits less clockwise rotation relative to FE-16, as shown in Fig. 15, suggesting a lower degree of shear deformation at the center. Conversely, the smaller grain sizes at the periphery of FE-22 indicate more pronounced shear introduction compared to FE-16. These divergent observations demonstrate that increased sticking conditions under higher extrusion forces do not correlate with a localized increase in shear deformation.

## Data availability

The data obtained from this research is available on ZENODO (10.5281/zenodo.19333062).

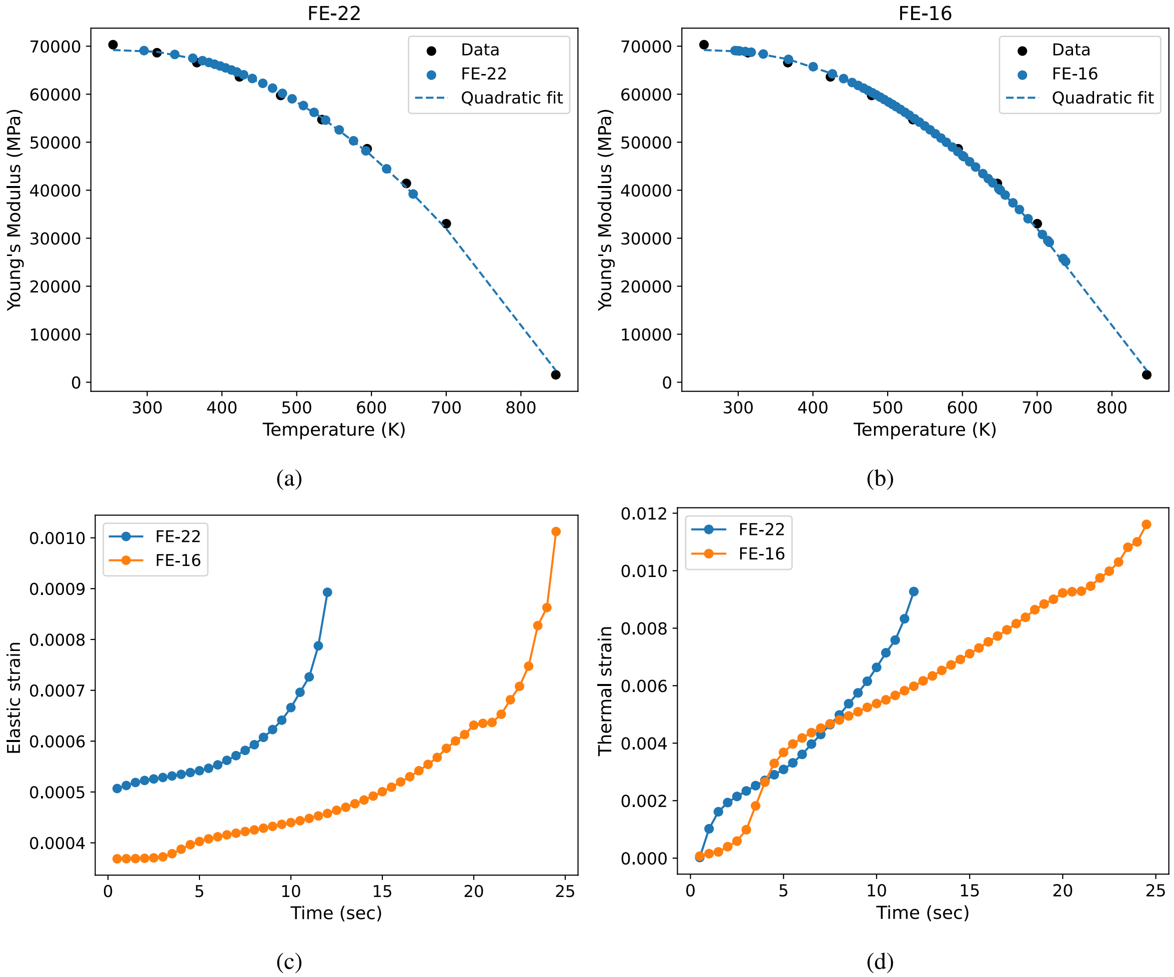

(a) (b) (c) (d)

**Fig. 20.** (a) Parametric fit of Young's modulus as a function of temperature for FE-22; (b) Parametric fit of Young's modulus as a function of temperature for FE-16; (c) Elastic strain during FE processes estimated from the measured load using the Young's modulus; (d) Thermal strain during FE processes obtained using Eq. (C.2).

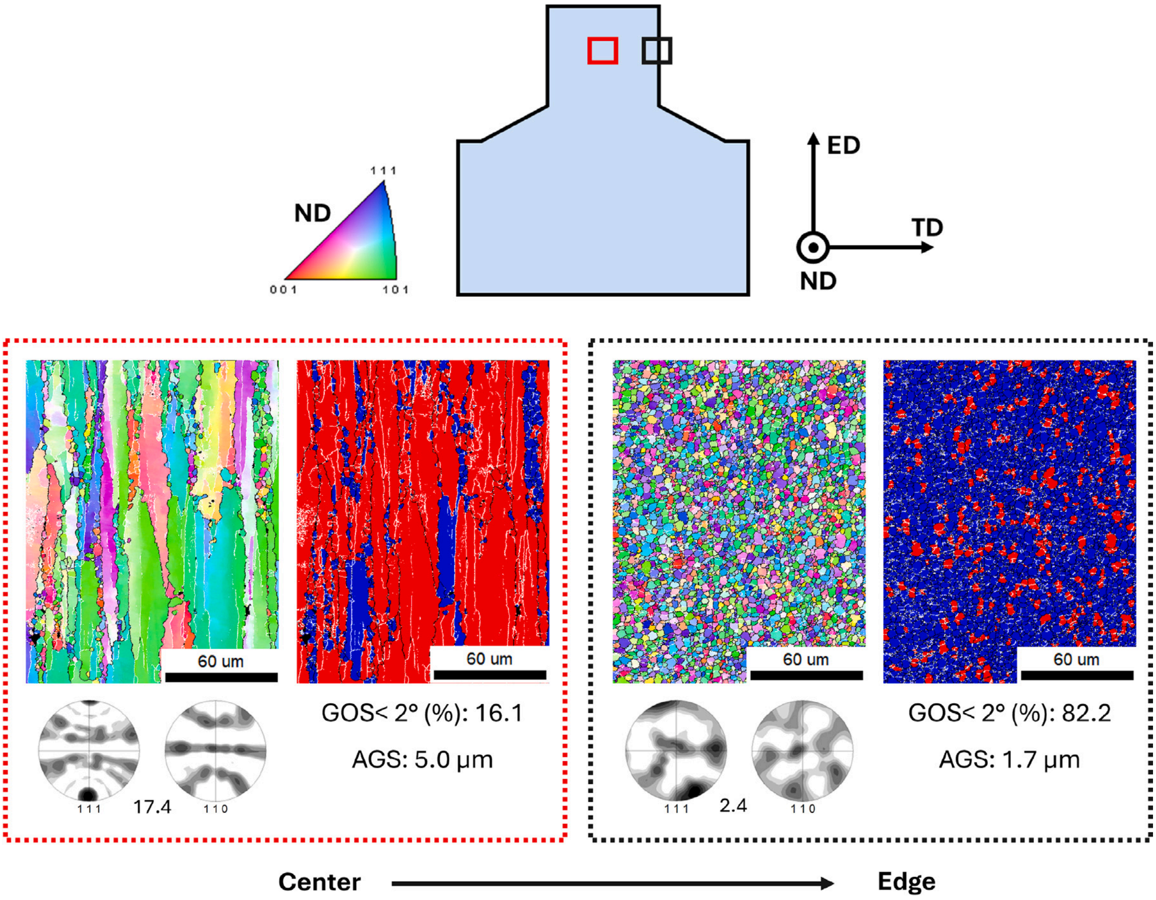

**Fig. 21.** Electron backscatter diffraction (EBSD) microstructural characterization of the extruded wire at 22 kN. Inverse pole figure (IPF) maps are shown for both the center and the edge regions of the specimens. The corresponding pole figures illustrate the texture evolution with the intensities in multiples of random distribution (mrd). The degree of recrystallization is represented in the fraction of grain orientation spread (GOS) <2°, and the average grain size was assessed by the high-angle grain boundaries (HAGBs) spacing perpendicular to extrusion direction (ED).

## References

[1] W.M. Thomas, E.D. Nicholas, S.B. Jones, 1993, US Patent: 5,262,123.

[2] W. Tang, AnthonyP. Reynolds, Production of wire via friction extrusion of aluminum alloy machining chips, J. Mater. Process. Technol. 210 (15) (2010) 2231–2237.

[3] D. Baffari, A.P. Reynolds, A. Masnata, L. Fratini, G. Ingarao, Friction stir extrusion to recycle aluminum alloys scraps: Energy efficiency characterization, J. Manuf. Process. 43 (2019) 63–69.

[4] G.K. Padhy, C.S. Wu, S. Gao, Friction stir based welding and processing technologies-processes, parameters, microstructures and applications: A review, J. Mater. Sci. Technol. 34 (1) (2018) 1–38.

[5] C.E.D. Rowe, WayneM. Thomas, Advances in tooling materials for friction stir welding, TWI Cedar Met. Ltd (2005) 1–11.

[6] Y. Yang, Z. Shen, P. Zhou, S. Guo, Y. Guo, W. Hou, Z. Piao, S. Yan, D. Liang, H. Li, Interfacial microstructure and mechanical performance of oscillating refill friction stir spot welded Al/Mg dissimilar welds, J. Manuf. Process. 158 (2026) 251–274.

[7] Z. Ma, R.S. Mishra, Development of ultrafine-grained microstructure and low temperature (0.48 Tm) superplasticity in friction stir processed Al–Mg–Zr, Scr. Mater. 53 (1) (2005) 75–80.

[8] Xiao. Li, Dario. Baffari, A.P. Reynolds, Friction stir consolidation of aluminum machining chips, Int. J. Adv. Manuf. Technol. 94 (2018) 2031–2042.

[9] W.M. Thomas, E.D. Nicholas, M. Gittos, Friction based technology for aluminium, Proc. Alum. 98 (1998).

[10] P. Aspes, Z. Kallien, L. Rath, U. Suhuddin, B. Klusemann, Effect of consumable stud microstructure on friction surfacing: Comparison between friction extruded and hot extruded AA2024 studs, J. Mater. Process. Technol. 341 (2025) 118862.

[11] Z. Shen, M. Zhang, D. Li, Z. Sun, W. Hou, Y. Tian, W.Y. Li, Microstructure evolution and mechanical properties of single-layer multipass overlapped Al–Mg–Mn–Sc–Zr alloy fabricated via additive friction stir deposition, Jom 75 (10) (2023) 4242–4253.

[12] Dario. Baffari, AnthonyP. Reynolds, Xiao. Li, Livan. Fratini, Influence of processing parameters and initial temper on Friction Stir Extrusion of 2050 aluminum alloy, J. Manuf. Process. 28 (2017) 319–325.

[13] RicardoM. Halak, Lars. Rath, UceuFHR. Suhuddin, JorgeF. dos Santos, Benjamin. Klusemann, Changes in processing characteristics and microstructural evolution during friction extrusion of aluminum, Int. J. Mater. Form. 15 (3) (2022) 24.

[14] X. Li, W. Tang, A.P. Reynolds, W.A. Tayon, C.A. Brice, Strain and texture in friction extrusion of aluminum wire, J. Mater. Process. Technol. 229 (2016) 191–198.

[15] Tianhao. Wang, JulianEscobar. Atehortua, Miao. Song, Md. Reza-E-Rabby, BrandonScott. Taysom, Josh. Silverstein, Timothy. Roosendaal, Darrell. Herling, Scott. Whalen, Extrusion of unhomogenized castings of 7075 aluminum via ShAPE, Mater. Des. 213 (2022) 110374.

[16] Scott. Whalen, Matthew. Olszta, Christian. Roach, Jens. Darsell, Daniel. Graff, Md. Reza-E-Rabby, Timothy. Roosendaal, Wayne. Daye, Tom. Pelletiers, Suveen. Mathaudhu, et al., High ductility aluminum alloy made from powder by friction extrusion, Materialia 6 (2019) 100260.

[17] Rajib. Kalsar, Xiaolong. Ma, Jens. Darsell, Dalong. Zhang, Keerti. Kappagantula, DarrellR. Herling, VineetV. Joshi, Microstructure evolution, enhanced aging kinetics, and mechanical properties of AA7075 alloy after friction extrusion, Mater. Sci. Eng.: A 833 (2022) 142575.

[18] JamesC. Williams, EdgarA. Starke Jr., Progress in structural materials for aerospace systems, Acta Mater. 51 (19) (2003) 5775–5799.

[19] J.P. Immarigeon, R.T. Holt, A.K. Koul, L. Zhao, W. Wallace, J.C. Beddoes, Lightweight materials for aircraft applications, Mater. Charact. 35 (1) (1995) 41–67.

[20] Susanne. Henninger, Rupesh. Chafle, Emad. Maawad, Benjamin. Klusemann, Martin. Müller, Peter. Staron, Impact of friction stir welding-like heat cycles on precipitates in AA7050 analyzed by SAXS and numerical modelling, Materialia (2025) 102343.

[21] W. Woo, Zhili. Feng, X.-L. Wang, D.W. Brown, B. Clausen, Ke. An, Hahn. Choo, CamdenR. Hubbard, StanA. David, In situ neutron diffraction measurements of temperature and stresses during friction stir welding of 6061-T6 aluminium alloy, Sci. Technol. Weld. Join. 12 (4) (2007) 298–303.

[22] JorgeF. Dos Santos, Peter. Staron, Torben. Fischer, JosephD. Robson, Aleksander. Kostka, P. Colegrove, Hua. Wang, Jakob. Hilgert, L. Bergmann, LeonLeander. Hütsch, et al., Understanding precipitate evolution during friction stir welding of Al–Zn–Mg–Cu alloy through in-situ measurement coupled with simulation, Acta Mater. 148 (2018) 163–172.

[23] J. Kieffer, D. Karkoulis, PyFAI, a versatile library for azimuthal regrouping, in: Journal of Physics: Conference Series, vol. 425, IOP Publishing, 2013, 202012.

[24] F. Zhang, J. Ilavsky, G.G. Long, J.P. Quintana, A.J. Allen, P.R. Jemian, Glassy carbon as an absolute intensity calibration standard for small-angle scattering, Met. Mater. Trans. A 41 (2010) 1151–1158.

[25] J.K. Park, A. Ardell, Microstructures of the commercial 7075 Al alloy in the T651 and T7 tempers, Met. Trans. A 14 (1983) 1957–1965.

[26] Malte. Storm, Gudrun. Lotze, pydidas - the python diffraction data analysis suite, 2025, https://github.com/hereon-GEMS/pydidas. (Acessed 5 May 2025).

[27] C. LLC, Introducing pandat software - an integrated modeling platform for materials design, 2025, https://computherm.com/. (Acessed 5 May 2025).

[28] W. Cao, S.-L. Chen, F. Zhang, K. Wu, Y. Yang, Y. Chang, R. Schmid-Fetzer, W. Oates, PANDAT software with PanEngine, PanOptimizer and PanPrecipitation for multi-component phase diagram calculation and materials property simulation, Calphad 33 (2) (2009) 328–342.

[29] T. Ohba, Y. Kitano, Y. Komura, The charge-density study of the Laves phases, MgZn2 and MgCu2, Cryst. Struct. Commun. 40 (1) (1984) 1–5.

[30] T. Rajasekharan, D. Akhtar, R. Gopalan, K. Muraleedharan, The quasi-crystalline phase in the Mg—Al—Zn system, Nature 322 (6079) (1986) 528–530.

[31] Z.-Z. Shi, W.-Z. Zhang, A transmission electron microscopy investigation of crystallography of $\tau$-Mg32 (Al, Zn) 49 precipitates in a Mg–Zn–Al alloy, Scr. Mater. 64 (2) (2011) 201–204.

[32] Y. Pan, X. Liu, H. Yang, Microstructural formation in a hypereutectic Mg–Si alloy, Mater. Charact. 55 (3) (2005) 241–247.

[33] S.C. Wang, M.J. Starink, Two types of S phase precipitates in Al–Cu–Mg alloys, Acta Mater. 55 (3) (2007) 933–941.

[34] A.L.M. Carvalho, L.B. Renaudin, A.J. Zara, J.P. Martins, Microstructure analysis of 7050 aluminum alloy processed by multistage aging treatments, J. Alloys Compd. 907 (2022) 164400.

[35] Jing-jing. Yu, Xiao-mei. Li, Xin-quan. Yu, Thermodynamic analyse on equilibrium precipitation phases and composition design of Al–Zn–Mg–Cu alloys, J. Shanghai Jiaotong Univ. (Sci.) 17 (2012) 286–290.

[36] B.E. Warren, X-ray Diffraction, Courier Corporation, 1990.

[37] Y. Zhao, J. Zhang, Microstrain and grain-size analysis from diffraction peak width and graphical derivation of high-pressure thermomechanics, Appl. Crystallogr. 41 (6) (2008) 1095–1108.

[38] N.H. Fletcher, Size effect in heterogeneous nucleation, J. Chem. Phys. 29 (3) (1958) 572–576.

[39] G. Sha, A. Cerezo, Early-stage precipitation in Al–Zn–Mg–Cu alloy (7050), Acta Mater. 52 (15) (2004) 4503–4516.

[40] G. Sha, Y. Wang, X. Liao, Z. Duan, S. Ringer, T. Langdon, Influence of equal-channel angular pressing on precipitation in an Al–Zn–Mg–Cu alloy, Acta Mater. 57 (10) (2009) 3123–3132.

[41] K. Tahmasbi, M. Mahmoodi, Evaluation of microstructure and mechanical properties of aluminum AA7022 produced by friction stir extrusion, J. Manuf. Process. 32 (2018) 151–159.

[42] Y. Chen, N. Gao, G. Sha, S.P. Ringer, M.J. Starink, Microstructural evolution, strengthening and thermal stability of an ultrafine-grained Al–Cu–Mg alloy, Acta Mater. 109 (2016) 202–212.

[43] M.J. Starink, L. Cao, P. Rometsch, A model for the thermodynamics of and strengthening due to co-clusters in Al–Mg–Si-based alloys, Acta Mater. 60 (10) (2012) 4194–4207.

[44] H. Zhang, X. Li, W. Tang, X. Deng, A.P. Reynolds, M.A. Sutton, Heat transfer modeling of the friction extrusion process, J. Mater. Process. Technol. 221 (2015) 21–30.

[45] X. Li, M. Reza-E-Rabby, A. Guzman, G. Grant, S. Mathaudhu, M. Hinton, A. Reynolds, Strain and strain rate in friction extrusion, J. Mater. Res. Technol. 20 (2022) 882–893.

[46] H. Schmidt, J. Hattel, J. Wert, An analytical model for the heat generation in friction stir welding, Modelling Simul. Mater. Sci. Eng. 12 (1) (2003) 143.

[47] Ø. Frigaard, Ø. Grong, O. Midling, A process model for friction stir welding of age hardening aluminum alloys, Met. Mater. Trans. A 32 (5) (2001) 1189–1200.

[48] Z.M. Zhang, Y.B. Yang, M. Meng, Hot deformation behavior of 7075 aluminum alloy bar compressed with different orientation at elevated temperature, Adv. Mater. Res. 217 (2011) 1729–1732.

[49] S. Senkova, O. Senkov, D. Miracle, Cryogenic and elevated temperature strengths of an Al–Zn–Mg–Cu alloy modified with sc and Zr, Met. Mater. Trans. A 37 (12) (2006) 3569–3575.

[50] M. Reimann, Keyhole Repair in Precipitation Hardening Aluminum Alloys Using Refill Friction Stir Spot Welding (Ph.D. thesis), Technischen Universität Hamburg, 2018.

[51] A. Deschamps, F. Livet, Y. Brechet, Influence of predeformation on ageing in an Al–Zn–Mg alloy—I. Microstructure evolution and mechanical properties, Acta Mater. 47 (1) (1998) 281–292.

[52] A. Deschamps, G. Fribourg, Y. Brechet, J.L. Chemin, C. Hutchinson, In situ evaluation of dynamic precipitation during plastic straining of an Al–Zn–Mg–Cu alloy, Acta Mater. 60 (5) (2012) 1905–1916.

[53] H. Zhang, X. Zhao, X. Deng, M.A. Sutton, A.P. Reynolds, S.R. McNeill, X. Ke, Investigation of material flow during friction extrusion process, Int. J. Mech. Sci. 85 (2014) 130–141.

[54] H. Zhang, X. Li, X. Deng, A. Reynolds, M. Sutton, Numerical simulation of friction extrusion process, J. Mater. Process. Technol. 253 (2018) 17–26.

[55] A. Bois-Brochu, C. Blais, F.A. Tchitembo Goma, D. Larouche, Modelling of anisotropy for Al–Li 2099 T83 extrusions and effect of precipitate density, Mater. Sci. Eng.: A 673 (2016) 581–586.

[56] C. Zhang, C. Wang, Q. Zhang, G. Zhao, L. Chen, Influence of extrusion parameters on microstructure, texture, and second-phase particles in an Al–Mg–Si alloy, J. Mater. Process. Technol. 270 (2019) 323–334.

[57] K. Huang, R. Loge, A review of dynamic recrystallization phenomena in metallic materials, Mater. Des. 111 (2016) 548–574.

[58] A. Heidarzadeh, S. Mironov, R. Kaibyshev, G. Çam, A. Simar, A. Gerlich, F. Khodabakhshi, A. Mostafaei, D. Field, J. Robson, A. Deschamps, P. Withers, Friction stir welding/processing of metals and alloys: A comprehensive review on microstructural evolution, Prog. Mater. Sci. 117 (2021) 100752.

[59] R. Zhang, J.-H. Zheng, J. Jiang, Dynamic recrystallisation: A quantitative study on grain boundary characteristics and dependence on temperature and strain rate in an aluminium alloy, Acta Mater. 278 (2024) 120266.

[60] Y. Wang, G. Zhao, X. Xu, X. Chen, Effect of extrusion parameters on microstructure, texture and mechanical property anisotropy of spray deposited 2195 Al–Li alloy profile, Mater. Sci. Eng.: A 818 (2021) 141406.

[61] Y.-j. Guo, J.-f. Li, D.-d. Lu, H. Ning, W. You, Y.-l. Chen, P.-c. Ma, X.-h. Zhang, Z.-r. Zeng, R.-f. Zhang, Effects of dynamic precipitation and processing parameters on dynamic recrystallization behavior of 2195 Al–Cu–Li alloy during hot compression, J. Mater. Eng. Perform. 31 (2022) 2743–2760.

[62] B. Von Guerard, H. Peisl, R. Zitzmann, Equilibrium vacancy concentration measurements on aluminum, Appl. Phys. 3 (1974) 37–43.

[63] W. Woo, Z. Feng, X.-L. Wang, K. An, C.R. Hubbard, S.A. David, H. Choo, In situ neutron diffraction measurement of transient temperature and stress fields in a thin plate, Appl. Phys. Lett. 88 (26) (2006).